Dynamical Drivers of the Exceptional Warmth over Siberia during the Spring of 2020

ANTHONY M. DEANGELIS,[a,b] SIEGFRIED D. SCHUBERT,[a,b] YEHUI CHANG,[a,c] YOUNG-KWON LIM,[a,d] RANDAL D. KOSTER,[a] HAILAN WANG,[e] AND ALLISON B. MARQUARDT COLLOW[a,d]

[a] *Global Modeling and Assimilation Office, NASA Goddard Space Flight Center, Greenbelt, Maryland*
[b] *Science Systems and Applications, Inc., Lanham, Maryland*
[c] *Morgan State University, Baltimore, Maryland*
[d] *University of Maryland, Baltimore County, Baltimore, Maryland*
[e] *Climate Prediction Center, NOAA/NWS/NCEP, College Park, Maryland*

(Manuscript received 19 May 2022, in final form 17 March 2023, accepted 21 March 2023)

ABSTRACT: Much of Siberia experienced exceptional warmth during the spring of 2020, which followed an unusually warm winter over the same region. Here, we investigate the drivers of the spring warmth from the perspective of atmospheric dynamics and remote influences, focusing on monthly-time-scale features of the event. We find that the warm anomalies were associated with separate quasi-stationary Rossby wave trains emanating from the North Atlantic in April and May. The wave trains are shown to be extreme manifestations of the dominant modes of spring subseasonal meridional wind variability over the Northern Hemisphere. Using a large ensemble of simulations from NASA's GEOS atmospheric model, in which the model is constrained to remain close to observations over selected regions, we further elucidate the remote drivers of the unusual spring temperatures in Siberia. In both April and May, the wave trains were likely forced from an upstream region including eastern North America and the western North Atlantic. Analysis with a stationary wave model shows that transient vorticity flux forcing over and downwind of the North Atlantic, which is strongly related to storm activity caused by internal variability, is key to generating the wave trains, suggesting limited subseasonal predictability of the Rossby waves and hence the exceptional Siberian warmth. Our observational and model analyses also suggest that anomalous tropical atmospheric heating contributed to the unusual warmth in Siberia through a teleconnection involving upper-troposphere dynamics and the mean meridional circulation. This tropical–extratropical teleconnection offers a possible physical mechanism by which anthropogenic climate change influenced the extreme Siberian warmth.

KEYWORDS: Asia; Rossby waves; Teleconnections; Extreme events; Temperature; General circulation models

1. Introduction

The first half of 2020 was marked by unusual warmth over much of northern Asia (Overland and Wang 2021; Ciavarella et al. 2021; Collow et al. 2022). Of particular note was the persistence of warm anomalies over central Siberia from the winter into the spring, exceeding 5°C over a large region (Fig. 1). Spring temperature extremes are especially impactful over this region due to their influence on agriculture, ecosystems, lifestyle, permafrost, and the subsequent summer fire season (e.g., Chen et al. 2016; Ciavarella et al. 2021). The year 2020 was no exception, with numerous devastating wildfires documented over Siberia during June (Ciavarella et al. 2021). It is therefore of considerable interest to better understand the underlying causes for the unusual spring Siberian warmth in 2020, given potential implications for the predictability of similar events in the future.

The persistence of temperature anomalies from winter to spring over Eurasia is not an unusual phenomenon. One possible explanation for the persistence is sea surface temperature (SST) anomalies. Specifically, a tripole pattern of persistent SST anomalies in the North Atlantic, characterized by a band of warm anomalies around 40°N and cool anomalies to the north and south, has been linked to warm conditions over central Eurasia persisting from winter to spring (Wu and Chen 2020; Meng et al. 2022). Indeed, January–March SST anomalies during 2020 show some evidence of this tripole pattern (Fig. 1a). However, the structure and magnitude of the anomalies do not persist into April and May (Figs. 1b and 2), suggesting other factors likely contributed to the persisting Siberian warmth. In contrast, tropical SSTs were characterized by more consistent anomalies during the first 5 months of 2020, with many regions remaining above average (Figs. 1 and 2). A long-term trend in spring tropical SSTs over 1981–2021 contributed substantially to the April and May 2020 SST anomalies (Fig. 2). In a recent study, Schubert et al. (2022, hereafter S22) show that the above-average tropical SSTs during January–March 2020 likely contributed to the unusual Northern Hemisphere warmth through modifications to the extratropical circulation. Whether the tropics also influenced the Siberian temperature anomalies during April–May, however, has not yet been explored.

A key feature of the April–May Eurasian near-surface temperatures during 2020, distinguishing them from the preceding winter, is the zonally asymmetric pattern of positive–negative–positive anomalies stretching from western Europe through

Supplemental information related to this paper is available at the Journals Online website: https://doi.org/10.1175/JCLI-D-22-0387.s1.

Corresponding author: Anthony M. DeAngelis, anthony.deangelis@nasa.gov

DOI: 10.1175/JCLI-D-22-0387.1

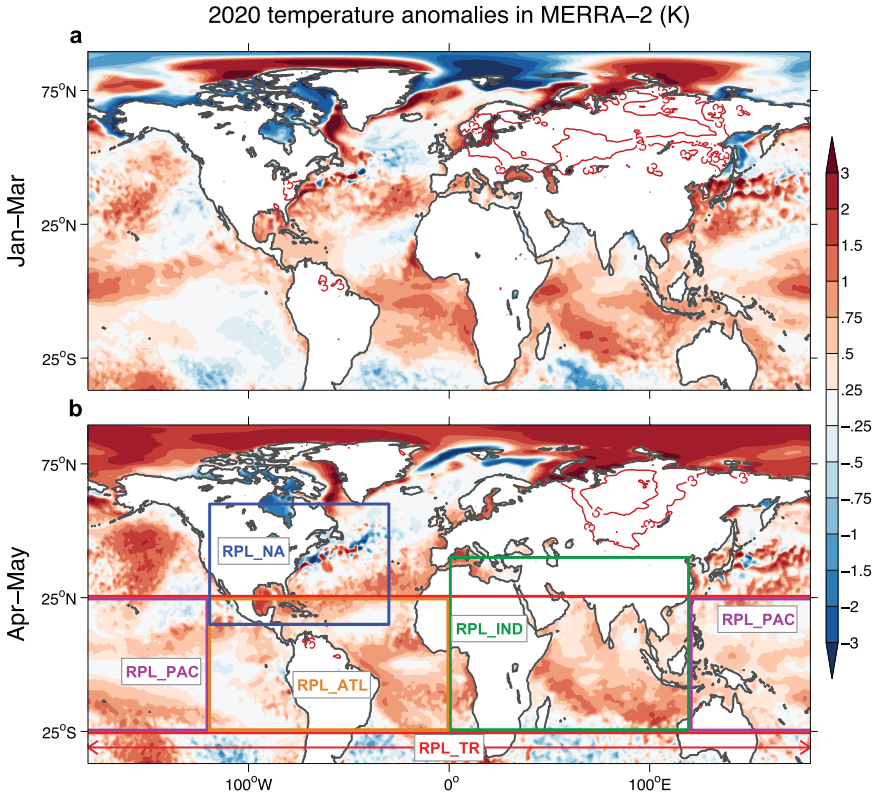

FIG. 1. MERRA-2 temperature anomalies during (a) January–March and (b) April–May 2020. SST anomalies (K) are shown as color fill over the oceans, and T2m anomalies are shown with red contours over land (contour lines drawn at 3 and 5 K, with negative contours omitted). Anomalies are relative to the 1981–2019 climatology of the corresponding months. The regions used to conduct regional replay simulations are shown in (b) (see Table 1 for region definitions).

Siberia, as seen with a Hovmöller diagram and spatial maps of 2-m temperature (T2m) anomalies (Figs. 3a and 4). The proximate cause of this anomaly pattern was the atmospheric circulation, with anomalies in upper-tropospheric eddy streamfunction (Ψ^e, where the eddy is computed by subtracting the zonal mean from the full streamfunction Ψ) corresponding in both location and sign with the underlying T2m anomalies (Figs. 3 and 4). The atmospheric circulation during this time is characterized by clear wave activity, with quasi-stationary Rossby wave trains (e.g., Hoskins and Ambrizzi 1993; Ambrizzi et al. 1995) emanating from the eastern North Atlantic (around 0°) through Eurasia (~100°E) in both April and May (Figs. 3b and 4). During April, a wave train appears to transfer its energy westward from Siberia toward western Europe during the first half of the month, then back eastward during the latter half of the month, resulting in two maxima in T2m and Ψ^e over Siberia in both early and late April (Fig. 3, outlined region). When applying a 15-day average, the spatial wave pattern is quite similar between the first and second halves of April over Eurasia, but a rather strong secondary positive Ψ^e anomaly also appears east of Greenland in late April (Figs. 4a,b). During May, the wave activity was somewhat more variable and less persistent than in April, with the absence of strong Ψ^e anomalies during the first 7–10 days of the month (Figs. 3b and 4c) followed by an apparently westward-shifting and intermittent wave train during the rest of the month (Fig. 3b). An average over 10–31 May shows a clearer wave signal, not unlike what occurred during April, but somewhat weaker and shifted to the west (Fig. 4d). The aforementioned Rossby wave trains during April and May, and their corresponding temperature anomalies, were associated with the negative phase of the wavelike Scandinavian teleconnection pattern (SCAND; Barnston and Livezey 1987; Overland and Wang 2021; Collow et al. 2022).

Recent studies point to additional factors that may have contributed to the unusual Siberian warmth during the spring of 2020. The Arctic Oscillation (AO) has been discussed as a likely contributing factor during April; it remained in a positive phase that month following its unusually strong magnitude during the prior winter (Overland and Wang 2021). While this may have certainly contributed to warmer temperatures across parts of the Northern Hemisphere, the AO weakened considerably in April,[1] suggesting the contribution was small. On a more local scale, land–atmospheric feedbacks were shown to be important later in the spring. In particular,

[1] https://www.cpc.ncep.noaa.gov/products/precip/CWlink/daily_ao_index/monthly.ao.index.b50.current.ascii.table.

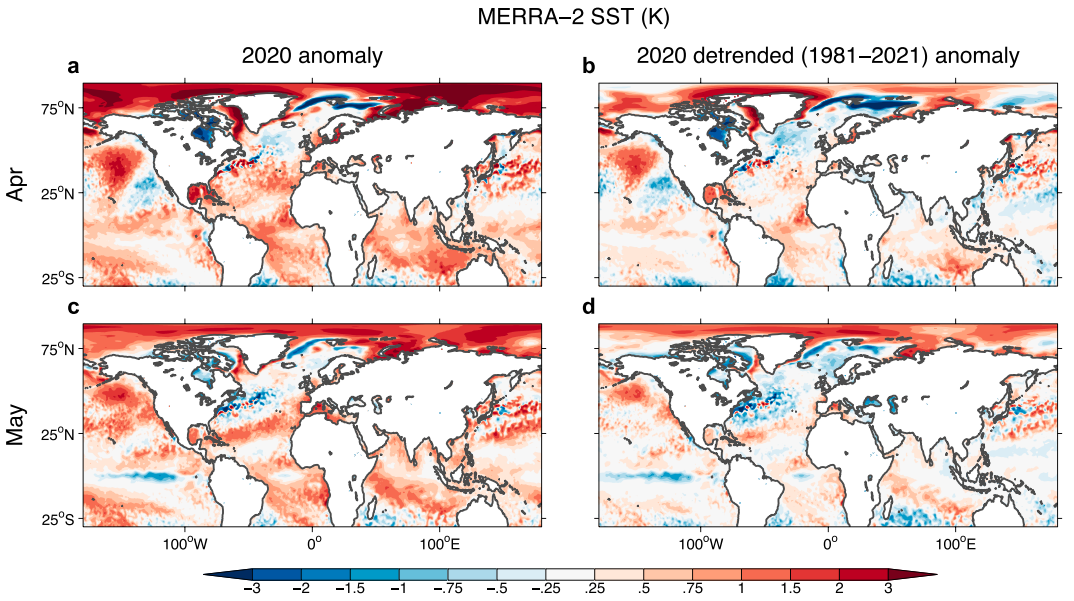

FIG. 2. MERRA-2 SST anomalies (K). (left) 2020 SST anomalies for (a) April and (c) May. Anomalies are relative to the 1981–2019 climatology of the corresponding month. (right) 2020 SST anomalies after removing the 1981–2021 linear trend for (b) April and (d) May.

low snow cover during May might have contributed as much as 20% to the above-average temperatures in Siberia then, owing to increased solar radiation through reduced surface albedo (Collow et al. 2022). Finally, a large deficit in upper-tropospheric–lower-stratospheric ozone, which shifted from the Arctic to Siberia from March through May, may also have contributed to April–May Siberian warmth through an increase in downwelling longwave radiation from high clouds (Xia et al. 2021).

While such mechanisms may have contributed to the unusual warmth over Siberia during the spring of 2020, a full understanding of the event, especially from the perspective of atmospheric dynamics, is lacking. Rossby wave trains clearly played a substantial role in the local temperature and circulation anomalies, and yet, the underlying forcing and statistical characteristics of those wave trains remain uncertain. Again, the possible impact of tropical SST (and atmospheric) anomalies on the spring circulation and Siberian warmth is essentially unexplored. Here, we address these gaps in understanding with a thorough analysis of observations and model simulations, focusing on monthly-time-scale features of the event. As a follow-up to S22, we utilize atmospheric general circulation model (AGCM) simulations with prescribed atmospheric conditions over various regions to elucidate the remote sources for the observed Rossby wave trains while simultaneously exploring the role of the tropics. The AGCM analysis is supplemented with simulations from a stationary wave model (SWM). To some degree, the analysis here may be considered an extension of S22 and complementary to Collow et al. (2022), aiming to complete our understanding of the mechanisms underlying the unusual Siberian warmth during early 2020 through a focus on the spring atmospheric dynamics. We will demonstrate that these dynamics were distinct from those of the prior winter and have potential implications for subseasonal prediction and climate change. The methodology, including observational data and model simulations, is described in section 2. Results are presented in section 3, and a summary and discussion are given in section 4.

2. Data and methodology

a. Observations

The Modern-Era Retrospective Analysis for Research and Applications version 2 (MERRA-2) is treated as a proxy for observations[2] in this study (Bosilovich et al. 2015, 2017; Gelaro et al. 2017). MERRA-2 is a state-of-the-art reanalysis produced by the National Aeronautics and Space Administration (NASA)/Goddard Space Flight Center (GSFC) Global Modeling and Assimilation Office (GMAO). This product assimilates conventional and satellite-based measurements (McCarty et al. 2016), including aerosol optical depth (Randles et al. 2016), into the GMAO's land–atmosphere modeling system [the Goddard Earth Observing System (GEOS) model (Molod et al. 2015)], providing data from 1980 through the present. We utilize numerous atmospheric fields from MERRA-2 (GMAO 2015a,b,c,d; Bosilovich et al. 2016), including precipitation that is corrected with gauge and satellite precipitation observations (Reichle and Liu 2014; Reichle et al. 2017). All MERRA-2 data are provided on a 0.625° longitude × 0.5° latitude grid.

[2] We will use the terminology "MERRA-2" and "observations" interchangeably throughout this paper, recognizing that reanalysis fields are not strictly observations.

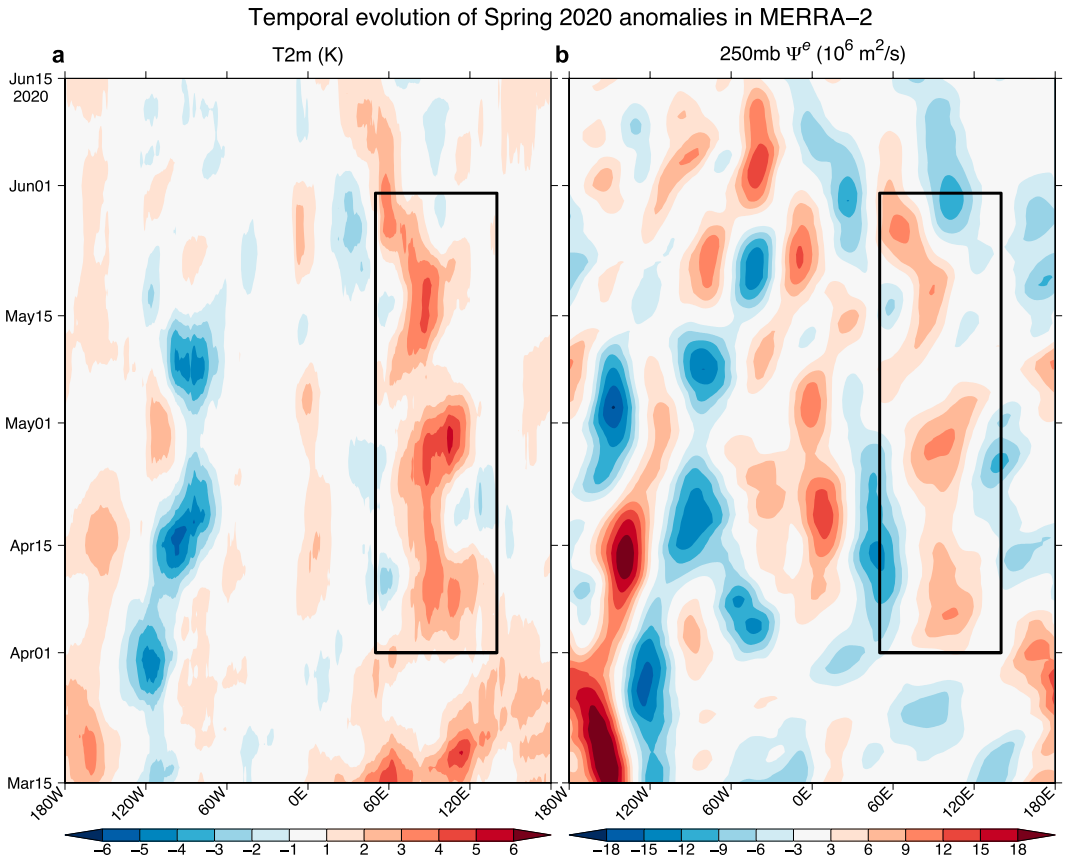

FIG. 3. Hovmöller diagram depicting the temporal evolution of (a) T2m (K) and (b) 250-mb eddy streamfunction (Ψ^e, 10^6 m^2 s^{-1}) anomalies in MERRA-2 during the spring of 2020. To compute Ψ^e, the zonal mean is removed from the full streamfunction (Ψ) anomaly field prior to plotting. Anomalies are relative to the 1981–2019 daily climatology and averaged over 30°–70°N. A 10-day running mean was applied to the fields for smoother plotting. The rectangles indicate the spatial and temporal domains of interest in this study: Siberia during April and May.

b. *Atmospheric model simulations*

We conduct numerous experiments with the GEOS AGCM to study the Eurasian temperature anomalies and their remote sources. The model version used here is the same as that used in the production of MERRA-2, but with two important differences: 1) the model is run here at a coarser 1° resolution (compared to the ~0.5° resolution used for MERRA-2), and 2) a tendency bias correction (TBC) procedure is implemented during the model runs to partially correct the model's climate biases (including subseasonal-to-seasonal variability) (Chang et al. 2019, 2021).[3]

We employ a "regional replay" approach in which the atmospheric conditions over selected regions of the globe are constrained to remain close to observations throughout the simulation while the remainder of the globe is unconstrained (Chang et al. 2019; Schubert et al. 2019b). Specifically, the AGCM's prognostic equations are modified over the replayed region to include an extra term: the difference between an analysis (here, MERRA-2) and a short-term (6-h) model forecast (the analysis increment). This forces the model to remain close to the analysis at each time step. In essence, the specifics of the weather simulated in the replayed region are forced to be consistent with MERRA-2. With this approach, one can assess (from the average of a large ensemble) whether the prescribed atmospheric forcing in a replayed region (e.g., the tropics) encouraged the development of anomalous atmospheric conditions in any of the free-running regions (e.g., Eurasia), thereby identifying the replayed region as an important source of remote forcing for those anomalous conditions through an atmospheric teleconnection mechanism. We should emphasize that the term "forcing" in this context refers to anomalous atmospheric dynamics and thermodynamics in the replayed region, which may be strongly influenced by internal atmospheric variability or linked with the underlying boundary conditions (i.e., SSTs). The regional replay approach was recently used to successfully diagnose remote sources of extreme events in the Northern Hemisphere, including for the winter preceding spring

[3] As described in Chang et al. (2019), the TBCs consist of time-averaged (over several decades) 6-hourly analysis increments (first guess forecast minus analysis) obtained from MERRA-2 data, which are added with opposite sign as additional forcing terms to the model equations.

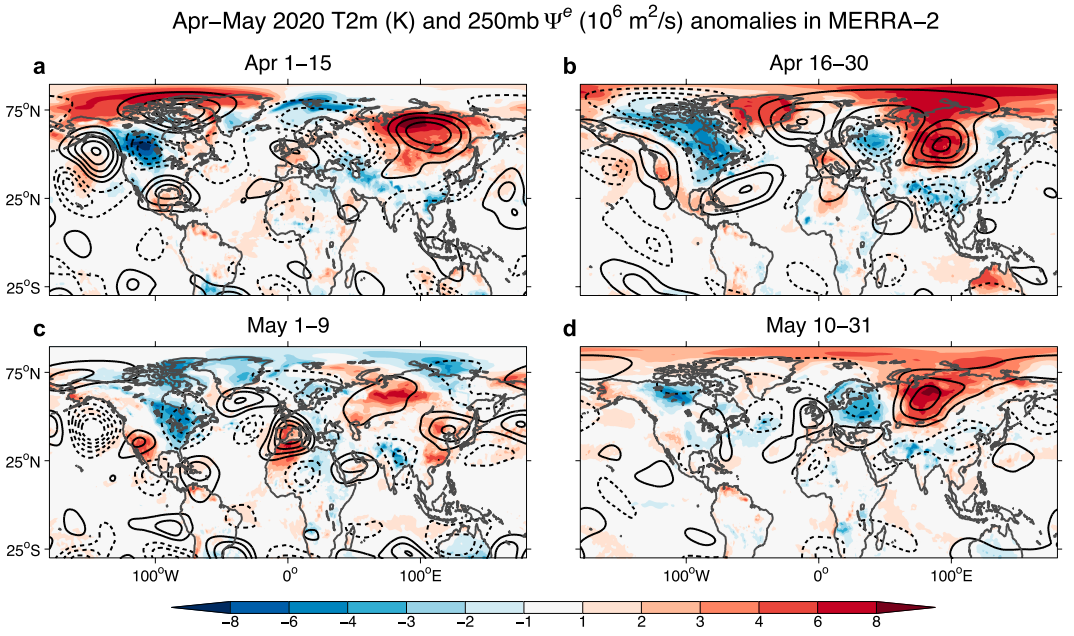

FIG. 4. Spatiotemporal evolution of T2m (shaded; K) and 250 mb Ψ^e (contoured; 10^6 m^2 s^{-1}) anomalies during April and May 2020 in MERRA-2. Anomalies are averaged over (a) 1–15 Apr, (b) 16–30 Apr, (c) 1–9 May, and (d) 10–31 May. 250-mb Ψ^e contours are drawn every 5×10^6 m^2 s^{-1}, with negative contours dashed and the zero contour omitted.

2020 (Schubert et al. 2021; S22). S22 provide additional discussion of the replay approach, including its comparison to "nudging."

The model runs utilized here are the same as those used in S22, with the addition of one replay region (Table 1). The runs are initialized at the end of 2018 and continued through the first half of 2020.[4] We generate 90 ensemble members for each selected replay region and an additional 90 members for the case with no regional replay (NORPL; i.e., a fully free-running AGCM simulation). Four of the selected regions are in the tropics, and one encompasses North America and the western North Atlantic (Fig. 1b; Table 1 provides region boundaries). The tropical regions are utilized to assess the degree to which the tropics (as a whole and from individual basins) contributed to the Eurasian temperature and circulation anomalies. The North American region is selected as a potential upstream extratropical source for the wave trains described in section 1 (e.g., Schubert et al. 2011; Chen et al. 2016, 2020). In all simulations, daily mean SST and sea ice concentration from MERRA-2 are prescribed everywhere around the globe (Gelaro et al. 2017). As discussed in S22, regional replay (especially in the tropics) influences the long-term model climatology with a tendency to warm the Northern Hemisphere extratropical land regions during the cool season. To generate 2020 anomalies that are not influenced by such replay-induced climate modifications, we also perform a parallel set of 39-yr runs (1981–2019, from which to compute a climatology) for each replay (and NORPL) experiment (Table 1).

c. *Analysis techniques*

For all analyses, anomalies are computed with respect to a 1981–2019 climatology. The anomaly for a given model experiment is computed by subtracting the experiment-specific climatology (e.g., NORPL_CLIM, RPL_TR_CLIM; see Table 1).

To quantitatively diagnose the presence and characteristics of wave trains, we apply a rotated empirical orthogonal function (REOF; Richman 1986) analysis to the MERRA-2 250-mb meridional wind (v250) data over the Northern Hemisphere (0°–89°N). Specifically, monthly mean April and May v250 anomalies over the period 1980–2021 are pooled for both months (resulting in 84 values at each grid cell: 42 years × 2 months per year) and subsequently fed into the REOF analysis. The anomalies are detrended (using the period 1980–2021) prior to performing the analysis. Rotation has been shown to result in EOF loading patterns that more closely resemble wave patterns and teleconnection features observed in nature and that are more robust (Barnston and Livezey 1987). We apply the REOF analysis to v250 (as opposed to other traditional fields such as geopotential height) to emphasize smaller zonal length scales (as v250 is proportional to the longitudinal derivative of geopotential height) and hence to maximize the

[4] This initialization is used because some of the runs are continuations of those used for a case study during the fall of 2019 (Schubert et al. 2021). For consistency, this same initialization was then used for all new runs for later case studies, including for S22 and this paper. Note that any initialization early enough to allow for the AGCM to establish its own climatology and variability (approximately 6 months or more prior to the analysis period) is sufficient.

TABLE 1. The AGCM experiments analyzed in this study. Atmospheric perturbations at the end of November 2018 were applied following Schubert et al. (2019a). All climatology experiments (indicated with _CLIM) are based on 39 individual runs, each initialized from MERRA-2 on 31 May of each year (1980–2018) and run through the following year (1981–2019). The first 10 months of each climatology run (previous June–March) are not used here.

Experiment	Simulation period	Replay region	No. of ensemble members
NORPL	30 Nov 2018–30 Jun 2020	None	90
RPL_TR	As in NORPL	Tropics: 25°S–25°N	90
RPL_PAC	As in NORPL	Tropical Pacific: 25°S–25°N, 120°E–120°W	90
RPL_ATL	As in NORPL	Tropical Atlantic: 25°S–25°N, 120°W–0°	90
RPL_IND	As in NORPL	Tropical Indian Ocean: 25°S–40°N, 0°–120°E	90
RPL_NA	As in NORPL	North America and western North Atlantic: 15°–60°N, 120°–30°W	90
NORPL_CLIM	1981–2019: a set of 39 separate runs initialized 31 May of each previous year	None	1
RPL_TR_CLIM	As in NORPL_CLIM	As in RPL_TR	1
RPL_PAC_CLIM	As in NORPL_CLIM	As in RPL_PAC	1
RPL_ATL_CLIM	As in NORPL_CLIM	As in RPL_ATL	1
RPL_IND_CLIM	As in NORPL_CLIM	As in RPL_IND	1
RPL_NA_CLIM	As in NORPL_CLIM	As in RPL_NA	1

presence of zonally propagating atmospheric wave activity in the leading REOF patterns (e.g., Schubert et al. 2011; Chen et al. 2020). Principal components (PCs) associated with the REOFs are computed traditionally by projecting the original input data (i.e., detrended v250 anomalies) onto the spatial loading patterns. PCs are also computed by projecting the full v250 anomalies (i.e., by removing the 1981–2019 climate, but without detrending) onto these loading patterns (herein PCAs, with the "A" here referring to the full anomaly). PCAs are generated for MERRA-2 anomalies as well as for AGCM anomalies. In the latter case, the AGCM anomalies for each experiment and ensemble member are projected onto the REOF loading patterns derived from the MERRA-2 data. As seen later, long-term trends in the MERRA-2 PCAs are insubstantial.

d. Stationary wave model analysis

The regional replay approach described in section 2b is limited in that it does not allow the explicit determination of the specific type of forcing (e.g., atmospheric diabatic heating, internal atmospheric dynamics) responsible for impacts downstream of the replayed regions. For a more controlled diagnosis of the forcing type, we conduct supplemental experiments with an SWM. The SWM used here is essentially the dry dynamical core of an AGCM; it is based on the primitive equations and applies damping such as Raleigh friction, Newtonian cooling, and biharmonic diffusion to suppress SWM-generated transients and ensure a stable and meaningful solution (Ting and Yu 1998). The model is baroclinic and time dependent and resolves stationary nonlinearity [i.e., it resolves nonlinear interactions associated with stationary waves (Ting et al. 2001)].

The SWM is global and run with rhomboidal wavenumber-30 truncation in the horizontal and 14 unevenly spaced sigma (σ) levels in the vertical. The prognostic variables are expressed in terms of anomalies relative to a three-dimensional time-mean basic state (here, computed as the 1980–2020 mean for April or May from MERRA-2). The model is initialized with small values of vorticity (ζ) at selected locations and has rigid boundaries at Earth's surface ($\sigma = 1.0$) and the top of the atmosphere ($\sigma = 0$); orography is accounted for through the hydrostatic equation. A steady solution is typically reached after about 30 days of integration; thus, we show results here for the average of days 31–59 of the simulations. For more details about the model, including the equations, see Ting and Yu (1998).

Following Schubert et al. (2011), we consider four types of forcing (again, forcing is interpreted here as anomalous atmospheric dynamics and/or thermodynamics) that can induce changes to the atmospheric circulation (and thus generate wave trains) in the SWM. These include total diabatic heating (Q, including condensation and radiation) and the convergence of transient fluxes of ζ, divergence (D), and temperature (T). The transient flux forcing, derived from the quadratic transient terms in the prognostic equations for ζ, D, and T (see Ting and Yu 1998), can be estimated from observational data as

$$\mathrm{TF}_{\mathrm{vor}} = -\boldsymbol{\nabla}\cdot\overline{\mathbf{V}'\zeta'}\,, \tag{1}$$

$$\mathrm{TF}_{\mathrm{div}} = \mathbf{k}\cdot\boldsymbol{\nabla}\times\overline{\mathbf{V}'\zeta'} - \frac{1}{2}\nabla^2(\overline{\mathbf{V}'\cdot\mathbf{V}'}), \quad \text{and} \tag{2}$$

$$\mathrm{TF}_{\mathrm{temp}} = -\boldsymbol{\nabla}\cdot\overline{\mathbf{V}'T'} - \frac{\partial(\overline{\omega'T'})}{\partial P} + \frac{R_d(\overline{\omega'T'})}{c_p P}, \tag{3}$$

where $\mathrm{TF}_{\mathrm{vor}}$, $\mathrm{TF}_{\mathrm{div}}$, and $\mathrm{TF}_{\mathrm{temp}}$ are the transient forcings for ζ, D, and T, respectively, and are imposed as constant forcing terms in the corresponding prognostic equations. In (1)–(3), $\mathbf{V}$ is the horizontal wind vector, ω is vertical pressure velocity, P is pressure, R_d is the gas constant for dry air, and c_p is the specific heat of air at constant pressure. Overbars represent monthly means, and the primes are high-frequency deviations of the respective variables from the monthly means. Here, we

compute the quantities in (1)–(3) from MERRA-2 pressure-level data using raw (i.e., with no filtering applied) 6-hourly instantaneous fields.

The Q forcing is computed from MERRA-2 as the sum of the total temperature tendency due to physics (i.e., the model-generated total diabatic heating) and the temperature tendency analysis increment (the difference between the short-term model forecast and analysis). The analysis increment is added to correct for possible errors in Q due to parameterization deficiencies in the AGCM underlying the reanalysis.[5] The Q forcing is monthly averaged and imposed as a constant forcing term in the SWM's prognostic T equation.

In addition to deriving the SWM forcing from actual data, we can also supply the SWM with idealized synthetic forcing in the prognostic equations. This exercise can be useful for identifying the forcing locations and/or patterns that are optimal for generating a particular atmospheric circulation or wave response. Here, we aim to identify and summarize the most important forcing locations for generating the observed Rossby waves in April and May of 2020 (Fig. 4). Previous work showed the importance of both ζ and Q forcing for generating quasi-stationary Rossby waves over Eurasia (Ding and Wang 2005; Schubert et al. 2014; Lim 2015; Ma and Franzke 2021). We thus focus on ζ and Q idealized forcing here. Following Schubert et al. (2014), the horizonal structure of the idealized forcing (imposed at a single location) has a sine-squared functional form with a horizonal length scale of 10° longitude × 10° latitude for ζ and 40° longitude × 10° latitude for Q. The vertical structure of the forcing follows Fig. 13 of Liu et al. (1998) and has a peak value of $\sim 5.4 \times 10^{-10}$ s^{-1} in the upper troposphere for ζ, and $\sim$3.1 K day^{-1} in the middle troposphere for Q [see also Eq. (4) of Ting and Yu (1998)].

To summarize the wave response to imposed idealized forcing at various locations, we generate a so-called "optimal forcing pattern" (OFP) for each type of forcing. As described in Schubert et al. (2011), this is accomplished by first conducting a series of SWM simulations where idealized ζ or Q forcing is imposed at regular intervals around the globe (every 10° longitude and 5° latitude), generating a library of responses to all possible forcing locations. Then, the normalized spatial inner product (NIP) is computed between each of the SWM responses and a target verification map (i.e., MERRA-2 observations) within a specified geographic region. Specifically, NIP is expressed as the following:

$$\mathrm{NIP} = \frac{\sum_{j=1}^{N} (\Psi^e_{S,j} \times \Psi^e_{V,j})}{\sqrt{\sum_{j=1}^{N} (\Psi^e_{S,j})^2} \sqrt{\sum_{j=1}^{N} (\Psi^e_{V,j})^2}}, \tag{4}$$

where $\Psi^e_{S,j}$ is the eddy streamfunction anomaly simulated by the SWM at grid cell j within the verification region, $\Psi^e_{V,j}$ is the verification eddy streamfunction anomaly at the same grid cell, and N is the total number of grid cells in the verification region. NIP is a unitless quantity. An NIP value closer to 1 indicates better agreement in the spatial pattern of Ψ^e anomalies between the SWM simulation and verification data; a value close to −1 indicates that the patterns are nearly opposite in sign. After the NIPs are computed for each of the idealized forcing simulations, they are displayed on a map at the locations corresponding to each of the idealized forcing locations, thus forming the OFP for a given forcing type. This map can be interpreted as the spatial pattern of forcing that is most ideal for generating the target wave response. Note, however, that the OFP is based purely on idealized simulations and thus exhibits a spatial pattern that is much smoother than typical forcing in the real world, especially for vorticity.

3. Results

In our subsequent results, we focus on the April and May monthly means for all findings related to the Rossby wave trains. This approach is justified because, as shown in section 1, the April wave train exhibits only minor submonthly variability (Figs. 3 and 4a,b), and during May, the signal is clearer for a longer-period average (Fig. 4d). Moreover, our intention here is not to thoroughly understand the synoptic meteorological evolution of the event, however interesting it may be. Rather, we aim to diagnose the dynamical mechanisms that manifest on somewhat longer (monthly) time scales. Given the similarity in our results for April and May, the following figures and discussion focus on April, for which the signals are also clearer. Results for May not shown here can be found in the supplemental material.

a. *Overview of AGCM results*

A comparison of the observed T2m and 250-mb Ψ^e anomalies for April 2020 with the results from selected regional replay AGCM experiments is shown in Fig. 5. Only RPL_NA reproduces the observed monthly mean wave train and associated temperature anomaly pattern over Eurasia, with the peak Ψ^e anomaly over Siberia being somewhat weaker and shifted south in the RPL_NA ensemble mean compared to observations (Figs. 5a,b). No obvious zonally asymmetric circulation anomaly pattern is generated in the RPL_TR or NORPL experiments over Eurasia (Figs. 5c,d). This suggests the Rossby wave train that was strongly associated with the April temperature anomalies was not forced from the tropics but rather from an upwind region over North America and the western North Atlantic. In particular, the corrected atmospheric forcing over the upwind region (again, with forcing referring to the day-to-day atmospheric dynamics and thermodynamics for April 2020 from MERRA-2) was critical for the generation of the wave train. Supplementary experiments with regional replay applied over the North Pacific were also evaluated to examine whether extratropical regions further upstream (note the wave train over the North Pacific in Fig. 5a) were ultimately linked to the forcing in the RPL_NA region and thus the Eurasia wave train (Table S1 in the online supplemental material). Those experiments provide no evidence of this, however, as the Eurasia

[5] A comparison of Q computed this way with Q computed as a residual in the thermodynamic equation (Schubert et al. 2011) shows very similar results (not shown), suggesting the method applied here (which is computationally more efficient) is adequate.

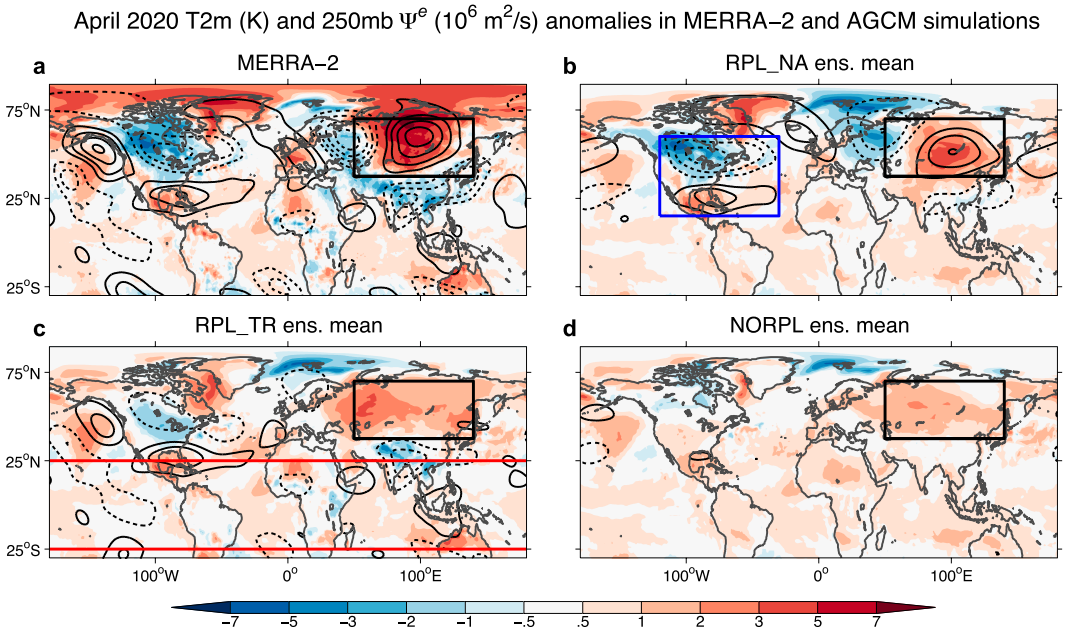

FIG. 5. April 2020 anomalies of T2m (shaded; K) and 250 mb Ψ^e (contoured; 10^6 m^2 s^{-1}) in (a) MERRA-2, (b) RPL_NA simulations, (c) RPL_TR simulations, and (d) NORPL simulations. The 90-member ensemble mean is shown for the AGCM results. All anomalies are relative to the corresponding MERRA-2 or AGCM experiment 1981–2019 April climatology (e.g., from RPL_NA_CLIM, RPL_TR_CLIM, etc.; see Table 1). The 250-mb Ψ^e contours are drawn every 4×10^6 m^2 s^{-1} with negative contours dashed and the zero contour omitted. Replayed regions are outlined in the colors corresponding to those in Fig. 1b. The region outlined in black over Asia (37.5°–70°N, 50°–140°E) is used for computing the AGCM ensemble probabilities in Table 2.

wave train is not captured even when the eastern North Pacific is replayed (Fig. S1).

The influence of Atlantic SSTs on the overlying atmospheric forcing that induced the April wave train remains unclear. On the one hand, if SSTs were important, we might expect a wave train to be generated in all experiments (as SSTs are prescribed in all runs), which is not the case. However, if SSTs were indeed important, the generation of the wave train would require the AGCM to correctly simulate both the atmospheric response to these SSTs and the persistence of the simulated wave train, neither of which is guaranteed. Therefore, the apparent unimportance of SSTs in our experiments could simply reflect model deficiencies. Additional AGCM experiments in which the SSTs were modified would be necessary to shed further light on this topic, but such experiments are beyond the scope of this study. The character of the atmospheric forcing in the spring of 2020, and its possible link with SST anomalies, will be further discussed with the SWM analysis in section 3c.

Despite not reproducing the wave train, RPL_TR exhibits a notable and relatively homogeneous warm anomaly over Eurasia in April 2020, with the largest anomalies being over the Ural Mountains (Fig. 5c). Substantial warm anomalies in RPL_TR are also found over the Labrador Sea and eastern North Pacific. The NORPL experiment produces a similar, but somewhat weaker, warm anomaly over Eurasia (Fig. 5d). That substantial warm anomalies appear over the Northern Hemisphere extratropics in RPL_TR suggests that a tropical–extratropical teleconnection process (apart from a wave train) acts to enhance the warm anomalies over Eurasia.

The observed and simulated anomalies for May 2020 are shown in Fig. 6 for the monthly average and in Fig. S2 for the period 10–31 May, during which the Eurasia wave train is more prominent. Qualitatively, the findings discussed above for April also apply for May; the wave train is only produced in the RPL_NA experiment (Figs. 6b and S2b), and there also appear to be tropically forced warm anomalies over the Northern Hemisphere (Figs. 6c and S2c).

The apparent influence of the tropics on the Eurasian T2m anomalies during April and May in the AGCM runs is worth further examination. As noted in section 1, tropical SSTs were generally above average during both months. In addition, the SST anomalies were associated with periods of above-average precipitation (P), with large zonal-mean P anomalies occurring just north of the equator from about mid-April through mid-May (Fig. S3a). Figure 7 shows the T2m and P anomalies in MERRA-2 and all tropical replay simulations during the period 15 April–15 May, which encompasses this tropical P peak. The results show robust positive T2m anomalies over Eurasia not only in the RPL_TR experiment but also when each individual tropical basin is replayed (Figs. 7b–e). In NORPL, both the tropical P and Eurasian T2m anomalies are weaker than in the replay experiments (Figs. S3c and 7f,l). These findings suggest a physical link between the tropical P anomalies (and their associated atmospheric heating) and the extratropical T2m anomalies. Although the

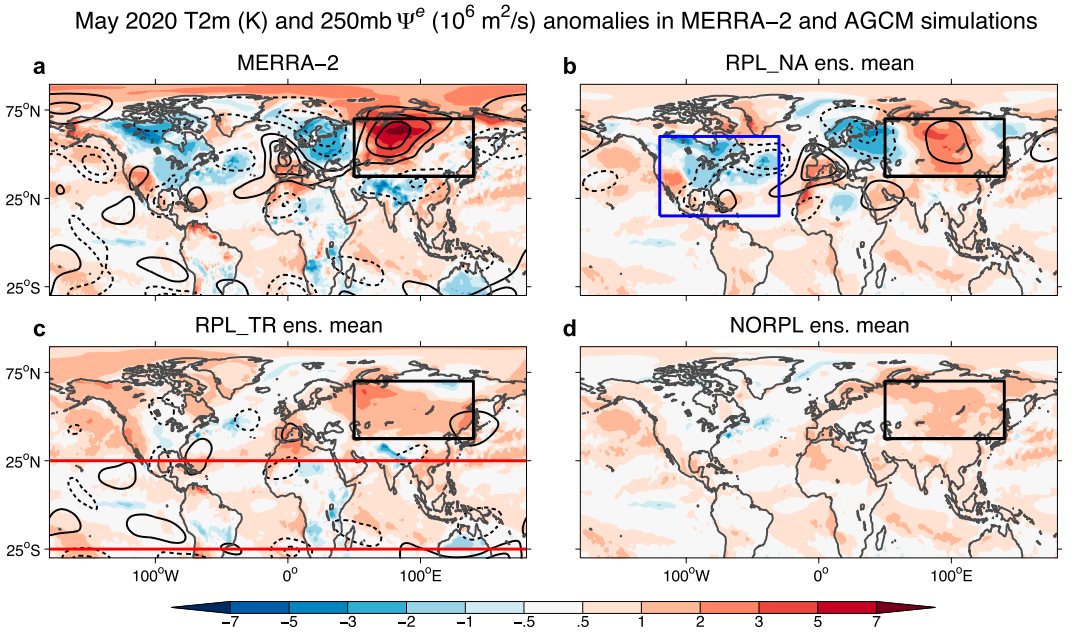

FIG. 6. As in Fig. 5, but for May 2020.

most widespread tropical *P* anomalies appear to be in the RPL_IND region, replay in any tropical basin evidently increases *P* across the entire tropics, resulting in larger *P* anomalies than NORPL in most places (Figs. 7g–l). This general enhancement of tropical *P* when any basin is replayed could explain why all tropical replay simulations have similar extratropical responses. In section 3d, the physical mechanisms connecting tropical heating in 2020 with the extratropical T2m are further explored.

To summarize, the AGCM results point to two important external sources for the unusual warmth over Siberia in both April and May: 1) atmospheric forcing over a region encompassing North America and the western North Atlantic that helped drive the Rossby wave trains that placed an upper-level anticyclonic anomaly over Siberia, and 2) forcing in the tropics, potentially influenced by above-average SSTs and precipitation, which caused warming over many parts of the Northern Hemisphere and presumably enhanced the warm anomalies over Eurasia related to the wave trains. An inspection of the ensemble-mean results (Figs. 5–7) suggests the tropics and upstream North America/North Atlantic region had a similar influence on the magnitude of temperature anomalies over Eurasia, with the latter more influential in the spatial pattern of T2m anomalies due to the presence of the wave trains. To quantify the contribution from both regions further, we examine the intraensemble variability in the RPL_NA and RPL_TR simulations and compare it with that in NORPL. Table 2 shows the probability of exceedance of various thresholds in the Siberia-averaged T2m *Z* score (i.e., T2m anomaly normalized by standard deviation; herein ZT2m) among the 90 ensemble members of the three experiments (see Table 2 caption for more details). Overall, the probability of ZT2m exceeding a given threshold within the Siberia region [the MERRA-2-computed area-mean ZT2m for April (1.31) or May (1.18), 1.5, or 1.0] is greatest for RPL_TR, with the probabilities for RPL_NA being similar to those for RPL_TR for the lower thresholds. In almost all cases, the probability of NORPL members having similarly extreme ZT2m values is the lowest among the experiments. These findings are consistent with the ensemble-mean results in Figs. 5–7, suggesting the tropics and upstream North America/North Atlantic provided additional forcing (beyond the prescribed SSTs) that was important for the extreme Siberian warmth and that both forcing regions contributed roughly equally.

b. Rossby wave trains quantified with REOF analysis

In this section, the Rossby wave trains in April and May of 2020 are examined with REOF analysis (section 2c) to address the following questions: To what extent were the wave trains manifestations of recurring modes of spring subseasonal (i.e., monthly) circulation variability? Was the amplitude of the wave trains (i.e., intensity of the troughs and ridges) extreme relative to other years over the recent historical record? Are the GEOS AGCM ensemble members capable of simulating wave train amplitudes that are consistent with observations when provided the 2020 upstream forcing in RPL_NA?

The spatial patterns of the leading REOF modes derived from MERRA-2 v250 data are displayed in Fig. 8. Rather than show the REOF loading patterns themselves for v250, we instead present the correlations between the associated PCs and basic variables (Ψ, T2m, and *P*). The first four modes represent wave trains impacting the North Atlantic and/or Eurasia, with the first and fourth modes representing wave trains over Eurasia that appear to originate from the eastern North Atlantic and extend to southeast Asia (Figs. 8a,j). REOF1 is characterized by anomalous anticyclones near the United Kingdom and

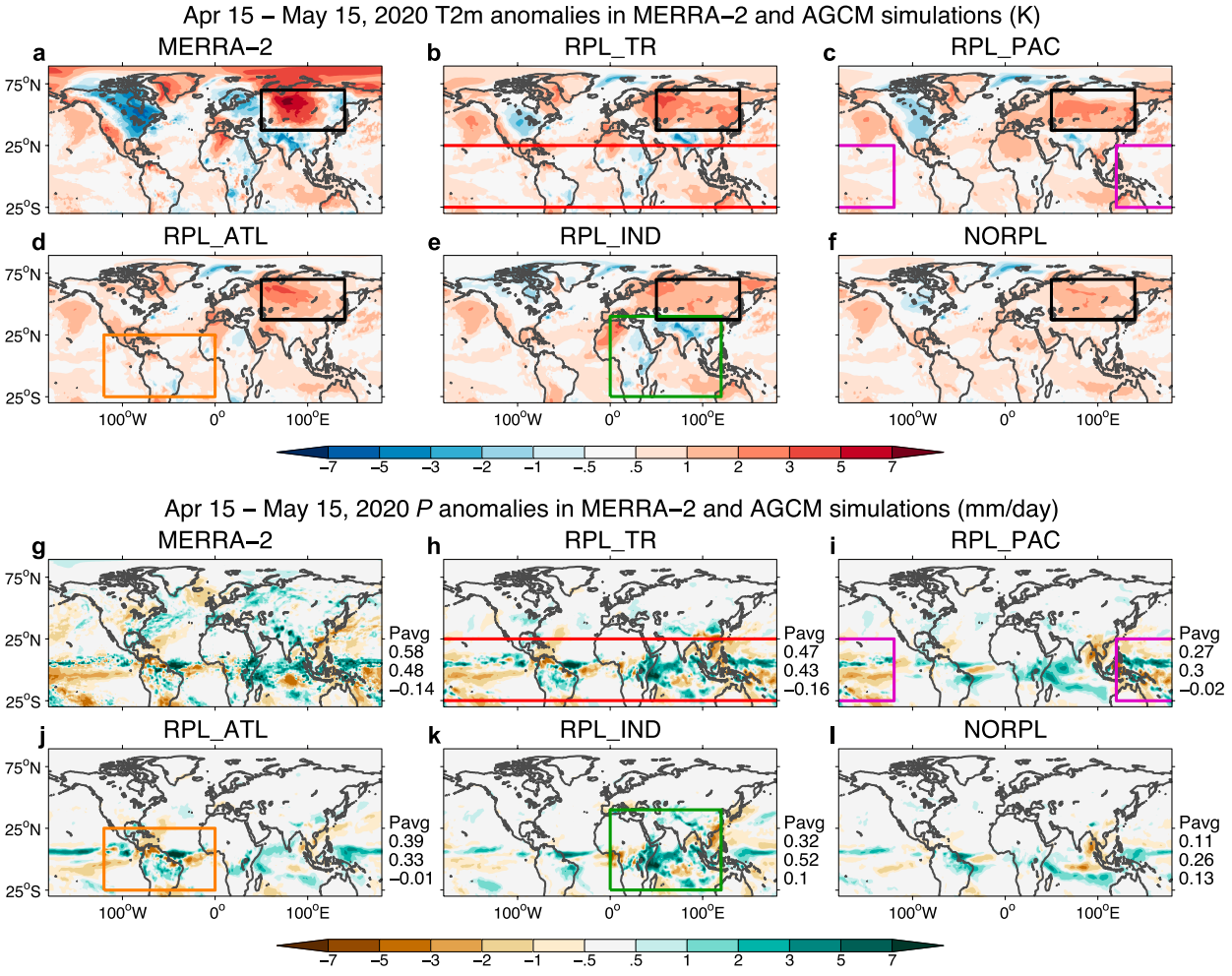

FIG. 7. Anomalies for the period 15 Apr–15 May 2020. T2m anomalies (K) are shown for (a) MERRA-2, (b) RPL_TR simulations, (c) RPL_PAC simulations, (d) RPL_ATL simulations, (e) RPL_IND simulations, and (f) NORPL simulations. (g)–(l) As in (a)–(f), but for precipitation (P) anomalies (mm day^{-1}). The 90-member ensemble mean is shown for the AGCM results. All anomalies are relative to the corresponding MERRA-2 or AGCM experiment 1981–2019 climatology for the period 15 Apr–15 May (see Table 1). Replayed regions are outlined in the colors corresponding to those in Fig. 1b. The region over Asia outlined in black in the T2m plots (37.5°–70°N, 50°–140°E) is the same as that in Figs. 5 and 6 for reference. The numbers to the right of each precipitation plot are the area-weighted average anomalies (Pavg) over the latitude ranges (from top to bottom for each panel) 0°–15°N, 7.5°S–7.5°N, and 15°S–0°.

central Siberia, with a notable cyclonic anomaly in eastern Europe. REOF4 is like REOF1 but is in quadrature with it and shifted somewhat north, with the strongest anticyclone over Eurasia instead being located over northwestern Russia (Fig. 8j). Together, these two modes suggest Eurasia wave trains are a typical manifestation of internal variability and that a wave train may look like either phase (positive or negative) of REOF1 or REOF4 or some combination of both.[6] Lagged correlations of PC1 and PC4 (e.g., April PC1 correlated with May PC4) are not statistically significant, indicating that these two REOF modes are not representing a preferred migration of one wave state to the other (e.g., a westward shift) between April and May. The Eurasia wave train modes are strongly associated with temperature anomalies, especially over Europe and Asia (Figs. 8b,k). This demonstrates the potential for these Rossby wave trains to induce heatwaves, such as that over Siberia during the spring of 2020, in a way consistent with earlier studies on the links between wave trains and extreme temperatures (e.g., Schubert et al. 2011; Fragkoulidis et al. 2018; Röthlisberger et al. 2019). The association of the four leading REOF modes with precipitation, while also having wave structures, is much weaker (Figs. 8c,f,i,l).

A cursory inspection suggests REOF1 closely resembles the observed wave train in April 2020 (cf. Figs. 5a and 8a). Indeed, the MERRA-2 PCAs (projections of the v250 anomalies onto

[6] A parallel analysis in which the REOFs are derived from large-ensemble long-duration NORPL AGCM runs (see Table S1) produced analogous Eurasia wave trains as modes 2 and 6 (not shown), but with a smaller difference in percent variance explained by the first six modes compared to MERRA-2 (ranging from 4.9% to 3.9%). This demonstrates the robustness of the Eurasia wave train modes across datasets.

TABLE 2. The fraction (F) of 90 ensemble members in which the area-weighted average ZT2m over a region encompassing Siberia (37.5°–70°N, 50°–140°E, indicated with the black box in Figs. 5–7) equals or exceeds various thresholds (the MERRA-2-computed area-mean ZT2m, 1.5, or 1.0). The area-weighted average ZT2m is computed by including only grid cells within the region in which ZT2m is positive. An ensemble member is considered to meet or exceed the threshold only if the area fraction of positive ZT2m values within the region also equals or exceeds 0.5. The MERRA-2-computed ZT2m is displayed in the heading for each month along with its rank among the years 1980–2021. The corresponding dataset climate (MERRA-2 or AGCM experiment) for the period 1981–2019 is used for computing ZT2m. Variations in the method (such as averaging over the entire region, computing the regional mean before the Z score, or removing the area fraction criterion for positive values) led to similar conclusions but generally smaller F values for RPL_NA. The method chosen above allows an ensemble member to have large positive ZT2m values over only part of the region (e.g., in the case of a wave train in RPL_NA) and still meet the threshold, enabling a fairer comparison among experiments.

	$F \geq$ MERRA-2 ZT2m	$F \geq 1.5$	$F \geq 1.0$
April 2020, MERRA-2 ZT2m = 1.31 (rank 2)			
NORPL	0.21	0.16	0.53
RPL_TR	0.44	0.23	0.77
RPL_NA	0.27	0.07	0.72
May 2020, MERRA-2 ZT2m = 1.18 (rank 2)			
NORPL	0.20	0.03	0.39
RPL_TR	0.44	0.08	0.68
RPL_NA	0.42	0.07	0.70

the REOFs) confirm that April 2020 was characterized by a strong manifestation of REOF1 (Fig. 9a). In fact, PCA1 for April 2020 was the largest over the period 1980–2021, highlighting the potency of this wave train then (Fig. 9c; Table 3). When considering the combined projection onto REOF1 and REOF4 (computed as $\sqrt{\text{PCA1}^2 + \text{PCA4}^2}$), which accounts for the possibility that a strong wave train may occur in any given year that resembles a combination of REOF1 and REOF4, April 2020 remains the most extreme (Fig. 9c; Table 3). The AGCM PCAs (projections of the AGCM v250 anomalies onto the REOF patterns) provide more evidence that RPL_NA is the most successful at reproducing the observed April 2020 wave train, with a much higher likelihood of the individual ensemble members having large PCA1 values compared to other replay experiments (Figs. 9a and S4a). However, no ensemble member simulates a wave train as strong as the observed (with all AGCM PCA1 values being smaller than the MERRA-2 PCA1). This may be partly due to AGCM biases in the mean jet stream, which can impact the wave train simulation (Wang et al. 2017). Additionally, it is possible that additional ensemble members are needed to capture the extreme nature of the wave train in the model.

The observed wave train in May 2020 closely resembles REOF4, i.e., a westward phase-shifted version of REOF1 (cf. Figs. 6a and 8j). Supporting this, the MERRA-2 v250 anomalies in May 2020 project rather strongly onto REOF4 (with PCA4 being about twice as large as PCA1; Fig. 9b). However, May 2020 is not an outlier within the context of the historical record (Fig. 9d), with PCA4 in 2020 being third largest and the combined projection onto REOF1 and REOF4 being fifth largest over 1980–2021 (Table 4). Considering the AGCM results, RPL_NA shows a clear shift toward more positive PCA4 values compared to other replay experiments (Figs. 9b and S4b), confirming again the importance of the upstream forcing over North America and the western North Atlantic for the generation of the May 2020 wave train. Several ensemble members (including those from RPL_NA, RPL_ATL, and RPL_IND) are capable of generating a wave train as strong as in MERRA-2 (with the AGCM PCA4 scatter encompassing the MERRA-2 PCA4 value; Figs. 6b and S4b), which partly reflects the weaker observed wave train in May compared to April.

In short, these results emphasize the unusual strength of the wave trains during the spring of 2020, particularly during April, making their contribution to the exceptional warmth over Siberia very likely. In Tables 3 and 4, we compare the statistics of the MERRA-2 PCAs with well-known indices of Eurasian atmospheric variability that represent wave trains. The findings confirm the robustness of the PCAs and highlight the strength of the 2020 wave trains across a variety of metrics. In particular, the east Atlantic–western Russia pattern (EAWR; Barnston and Livezey 1987; Lim 2015) index is highly correlated with PCA1 in April and had a large magnitude in 2020 compared to the previous four decades (Table 3). In May, the SCAND (Barnston and Livezey 1987; Lim 2015) and Eurasia teleconnection pattern (EU; Wallace and Gutzler 1981) are strongly related to PCA4 and had their largest and third largest index magnitudes in 2020, respectively, over the period 1980–2021 (Table 4).

c. *Wave train analysis with a stationary wave model*

Here, we use SWM experiments (section 2d) to further investigate the forcing for the 2020 springtime Eurasia wave trains. Figure 10b shows the OFP for ζ associated with the April 2020 wave train. The OFP can be interpreted as the locations and corresponding signs of upper-tropospheric ζ forcing (such as from TF_{vor}) that, if imposed over those locations, would induce an upper-tropospheric wave pattern over Eurasia that resembles that in MERRA-2 (Fig. 10a). In other words, positive ζ forcing over the regions in Fig. 10b colored in red would tend to produce a Eurasia wave train that is in phase with that in Fig. 10a and similarly for negative ζ forcing over the regions in blue. The results suggest that areas of positive and negative TF_{vor} both over and upstream of Eurasia (including the North Atlantic and southeast North America) can induce the observed Rossby wave train (Fig. 10b). The actual upper-tropospheric TF_{vor} forcing computed for April 2020 reveals a rather noisy field of both positive and negative values across the Northern Hemisphere, with particularly large positive values over parts of the North Pacific and Atlantic Oceans (Fig. 10c). To highlight the locations where the observed TF_{vor} would have been conducive for the 2020 wave train development, we multiply TF_{vor} by the OFP. The resulting field reveals several regions over the North Atlantic and Europe that were potential wave sources for the Eurasia wave train (small regions colored in red in Fig. 10d). When forcing the SWM with the TF_{vor} anomalies over a region extending

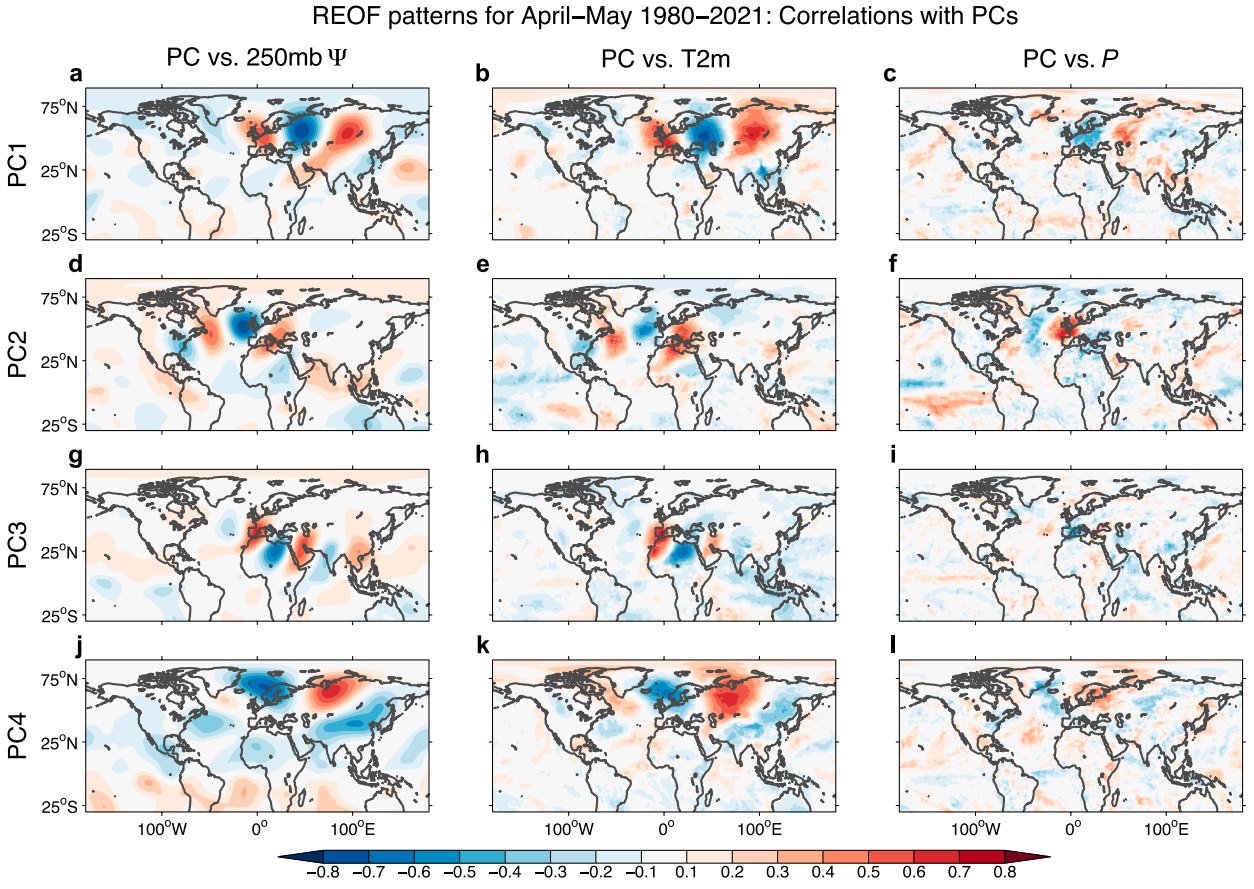

FIG. 8. The relationship between basic variables and the leading REOFs derived from the April and May 250-mb meridional wind (v250) monthly MERRA-2 data for 1980–2021. (a)–(c) Correlations between the principal components of the first REOF (PC1) and (left) 250-mb Ψ, (center) T2m, and (right) *P*. (d)–(f) As in (a)–(c), but for PC2. (g)–(i) As in (a)–(c), but for PC3. (j)–(l) As in (a)–(c), but for PC4. Each correlation map is computed from 84 values (42 years × 2 months). Correlations greater than magnitude 0.3 are statistically significant at the 1% level based on a two-tailed *t* test. MERRA-2 data were detrended for each month prior to performing the REOF analysis. The percentage of variance explained by each of the first four REOFs is 8.39%, 7.65%, 5.83%, and 5.43%, respectively.

from the North Atlantic to western Europe (magenta box in Fig. 10c), we find that the SWM produces a wave train over Eurasia that qualitatively resembles the observations (Fig. 10e). An SWM simulation that is forced with all April 2020 forcing (TF_{vor}, TF_{div}, TF_{temp}, and Q anomalies) in this region shows a similar response (Fig. 10f), indicating that the TF_{vor} forcing dominates. Analogous results for May 2020 show that TF_{vor} is again the dominant forcing source (Fig. S5).

Additional analysis was performed to evaluate the sensitivity of the SWM-simulated wave train to the exact region over which TF_{vor} forcing is applied. For both April and May 2020, we find that TF_{vor} over western Europe (especially near the United Kingdom; Figs. 10d and S5d) is necessary for the SWM to generate a wave train that is both sufficiently strong and has the same phase as the observed wave train (not shown). Although forcing over the central North Atlantic alone is insufficient for generating realistic wave trains in the SWM, this does not contradict our prior AGCM results showing the importance of prescribed forcing over the central North Atlantic (Figs. 5b and 6b). This is partly because, by design, the SWM suppresses the development of transient eddy feedbacks and therefore represents only the direct response to the given forcings (Ting and Yu 1998). In other words, the SWM is not necessarily representative of the real atmosphere and cannot be directly compared with a full AGCM that presumably includes realistic transient eddy feedbacks; the SWM should only be regarded as a tool to diagnose the types and regions of forcing that are important for a given background atmospheric state. Taken together, our SWM and AGCM results imply that TF_{vor} forcing over western Europe was likely generated as a dynamical feedback to the forcing upstream (i.e., between North America and the central North Atlantic) and that the forcing both upstream (which is constrained in the RPL_NA runs) and downstream (generated by the free-running AGCM) was important for the development of the Eurasia wave trains.

Given the importance of TF_{vor} forcing for the April and May wave trains in 2020, the mathematical and physical interpretations of this forcing deserve further elaboration. Mathematically, TF_{vor} is positive where there is convergence of a theoretical vector field representing the covariance of high-

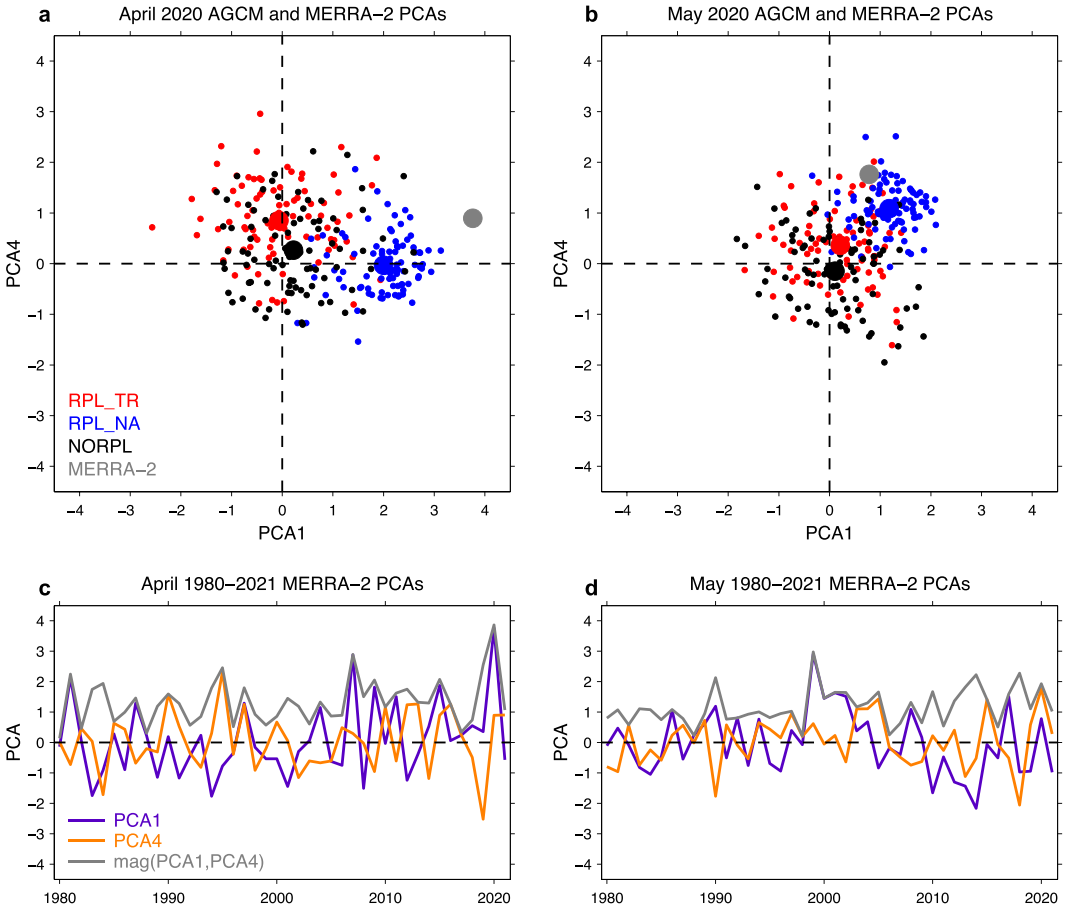

FIG. 9. Projections of AGCM and MERRA-2 v250 anomalies (PCAs) onto the REOF patterns derived from MERRA-2 (shown in Fig. 8). (a) Scatterplot of PCA4 vs PCA1 for April 2020 for the AGCM individual ensemble members (small dots) and ensemble mean (large dots) of each experiment (colors indicated in key). The corresponding MERRA-2 PCAs are indicated with the large gray dots. (b) As in (a), but for May 2020. (c) Time series of MERRA-2 PCAs for April 1980–2021 for PCA1 (purple), PCA4 (orange), and $\sqrt{\text{PCA1}^2 + \text{PCA4}^2}$ (gray; representing the distance from the origin to the point {PCA1, PCA4} on a scatterplot). (d) As in (c), but for May 1980–2021.

frequency (i.e., 6 hourly) vector wind and ζ anomalies. Since TF_{vor} appears in the SWM equation for ζ tendency (Ting and Yu 1998), positive TF_{vor} causes an increase in ζ (i.e., cyclonic motion). Taking the inverse Laplacian of TF_{vor} ($\nabla^{-2}\text{TF}_{\text{vor}}$) can aid with the interpretation of how TF_{vor} affects the circulation, which has the effect of smoothing and reversing the sign of the TF_{vor} field and converting it from a forcing of ζ tendency to that of Ψ tendency. Figure 11a shows that 250-mb $\nabla^{-2}\text{TF}_{\text{vor}}$ was large and negative during April 2020 over the North Atlantic around 50°N, inducing a decrease in Ψ there. Thus, TF_{vor} over the North Atlantic was evidently important for causing an initial cyclonic anomaly upstream of Eurasia that likely interacted with the background flow and formed a wave train further downstream. Areas of positive $\nabla^{-2}\text{TF}_{\text{vor}}$ anomalies over Eurasia coincide with positive anomalies of Ψ^e over the same regions (cf. Figs. 10a and 11a) and reflect a potential feedback between TF_{vor} and the wave train itself once it developed.

From physical and meteorological perspectives, TF_{vor} is closely related to storm activity. Figure 11c shows that the 250-mb zonal wind (u) was much above average over and to the east of the United States in April 2020, just south of the negative $\nabla^{-2}\text{TF}_{\text{vor}}$ anomalies (cf. Figs. 11a,c). Stronger upper-tropospheric winds are often associated with tighter tropospheric temperature gradients (due to the thermal wind balance) and potentially increase upper-tropospheric forcing for rising motion, both of which contribute to enhanced baroclinicity and storm development. As a metric of storm activity, we show the variance of 850-mb 6-hourly meridional wind [var(v)] in Fig. 11e. Positive anomalies in 850-mb var(v) were evident off the east coast of the United States and the North Atlantic around 50°N, in the vicinity of the aforementioned anomalies in 250-mb u and $\nabla^{-2}\text{TF}_{\text{vor}}$. These 850-mb var($v$) anomalies are consistent with more frequent and/or intense fluctuations in v speed and/or direction and hence increased storm frequency and/or intensity. Our results thus support a link between the observed TF_{vor} forcing and enhanced storminess in April 2020. A similar connection between the April 2020 Eurasia wave train, upstream TF_{vor}, and North

TABLE 3. Summary of Eurasia wave train indices for April. The indices summarized are, from top to bottom, PCA1 and PCA4 computed from MERRA-2 (shown in Fig. 9c), the east Atlantic–western Russia index (EAWR), the Scandinavian index (SCAND), the Eurasia teleconnection pattern (EU), the quantity $\sqrt{\text{PCA1}^2 + \text{PCA4}^2}$ [mag(PCA1, 4), shown in Fig. 9c], and $\sqrt{\text{EAWR}^2 + \text{SCAND}^2}$ [mag(EAWR, SCAND)]. The second column shows the 2020 rank of the magnitude of each index for the period 1980–2021 (ranks in square brackets for EAWR and SCAND are for 1950–2021). Correlations between each index and every other index are shown, with statistically significant correlations (based on a two-tailed t test) indicated with a single ($\alpha = 0.05$) or double ($\alpha = 0.01$) asterisk. The EAWR and SCAND indices were obtained from the NOAA CPC (https://www.cpc.ncep.noaa.gov/data/teledoc/telecontents.shtml). The EU index was computed from MERRA-2 as [−0.25 × ZH500(55°N, 20°E) + 0.5 × ZH500(55°N, 75°E) − 0.25 × ZH500(40°N, 145°E)], where ZH500 is the normalized (Z score) 500-mb geopotential height anomaly based on the local monthly climatological mean and standard deviation (Wallace and Gutzler 1981).

		Correlation with …					
Index	2020 rank	PCA1	PCA4	EAWR	SCAND	EU	mag(PCA1, 4)
PCA1	1						
PCA4	15	−0.07					
EAWR	3 [5]	0.80**	−0.43**				
SCAND	5 [6]	−0.39*	−0.63**	0.00			
EU	13	−0.02	0.71**	−0.31*	−0.63**		
mag(PCA1, 4)	1	0.48**	0.09	0.22	−0.19	0.11	
mag(EAWR, SCAND)	2 [4]	0.38*	0.06	−0.04	−0.17	0.23	0.58**

Atlantic storminess is found in the free-running AGCM (Figs. 11b,d,f), suggesting the GEOS model is able to adequately capture the dynamics underlying the wave train forcing. Analogous results for May 2020 are qualitatively similar to those for April, albeit with weaker $\nabla^{-2}\text{TF}_{\text{vor}}$ anomalies in the North Atlantic (Fig. S6). The anomalous North Atlantic storminess in the spring of 2020 was potentially linked to the underlying SSTs, which show an anomalous north–south temperature gradient over the North Atlantic during both April and May (Figs. 2a,c). Such a link between SST gradients, low-level baroclinicity, and the generation of transient eddy Rossby wave sources in the North Atlantic has also been noted in previous studies (Liu et al. 2014; Zhang et al. 2022).

We now briefly turn to an analysis of the diabatic heating or Q forcing associated with the spring 2020 Rossby waves. The SWM-derived OFP for Q suggests midtropospheric forcing over the North Atlantic may also contribute to the production of an upper-tropospheric wave train over Eurasia (Fig. 12b), though this contribution is somewhat weaker than that for vorticity (Fig. 10b). Positive Q anomalies were evident during April 2020 over the western North Atlantic (Fig. 12c). These anomalies may have arisen from a couple of factors: 1) condensational heating associated with anomalous clouds and precipitation due to enhanced storm activity (e.g., Fig. 11; Pfahl et al. 2014; Binder et al. 2016), or 2) large-scale anomalies in sensible and latent heat flux (the latter also linked to precipitation) that are more directly associated with anomalously warm SSTs (Fig. 2a; Chen et al. 2016, 2020). When the observed Q forcing is imposed in the SWM, however, little or no circulation response occurs over Eurasia compared to when all forcings are imposed (Figs. 12e,f), suggesting the Atlantic Q anomalies were inconsequential for the wave train development. This implies the thermodynamic anomalies associated with enhanced transients and storm activity over the North Atlantic, which enter the SWM through the T tendency equation here, were much less important than the direct dynamical contributions from these transients. The results for May are qualitatively similar, but with weaker observed Q anomalies over the North Atlantic (Fig. S7).

Finally, we explore the question of whether the dominance of TF_{vor} forcing in 2020 was an unusual characteristic for that particular year or is representative of typical historical spring Eurasia wave trains. To assess this, we generate forcing maps representing the anomalies of a given forcing (e.g., TF_{vor}, Q) typically associated with Eurasia wave trains and then impose those forcing patterns on the SWM. Specifically, a forcing map is generated by first pairing the MERRA-2 forcing anomalies over 1980–2021 at each grid cell with the corresponding PCA values for a given Eurasia wave train REOF mode (shown in Figs. 9c,d) and then calculating for that grid

TABLE 4. As in Table 3, but for May.

		Correlation with …					
Index	2020 rank	PCA1	PCA4	EAWR	SCAND	EU	mag(PCA1, 4)
PCA1	21						
PCA4	3	0.10					
EAWR	29 [45]	0.80**	−0.10				
SCAND	1 [1]	−0.10	−0.79**	−0.01			
EU	3	0.04	0.63**	0.05	−0.70**		
mag(PCA1, 4)	5	0.23	−0.09	0.19	−0.11	0.03	
mag(EAWR, SCAND)	2 [3]	0.02	0.01	−0.11	−0.14	0.04	0.51**

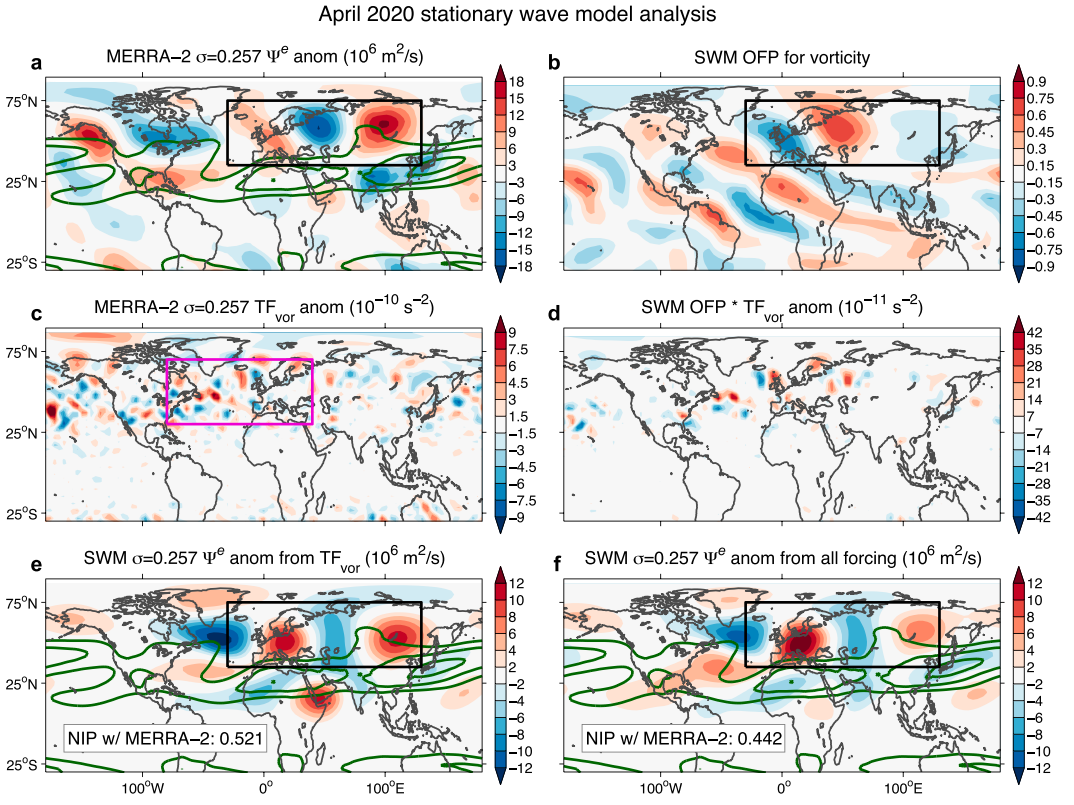

FIG. 10. Analysis of the April 2020 wave train with an SWM. (a) Verification: MERRA-2 April 2020 Ψ^e anomaly at sigma level (σ) 0.257 (10^6 m^2 s^{-1}). Green contours indicate the $\sigma = 0.257$ basic-state zonal wind (u; contour interval: 10 m s^{-1}, starting at 20 m s^{-1}). (b) OFP for vorticity forcing based on the verification in (a) (unitless). The verification domain (35°–75°N, 30°W–130°E) is indicated with the black box in (a) and (b). (c) MERRA-2 April 2020 anomaly of transient vorticity flux convergence (TF_{vor}) at $\sigma = 0.257$ (10^{-10} s^{-2}). (d) The product of the TF_{vor} anomaly in (c) with the OFP in (b). (e) Ψ^e anomaly at $\sigma = 0.257$ from the SWM when forced with the observed TF_{vor} anomalies over the region outlined in the magenta box (30°–70°N, 80°W–40°E) in (c). Note that TF_{vor} anomalies over the entire depth of the troposphere are used as forcing for the SWM to produce (e). The SWM output is averaged over days 31–59 of the simulation. The unitless normalized inner product (NIP) between the SWM output and MERRA-2 verification over the region outlined in the black box is printed in the bottom left of the panel. (f) As in (e), but for the SWM output when forced with April 2020 anomalies of all transient flux (TF_{vor}, TF_{div}, TF_{temp}) and diabatic heating (Q) forcing computed from MERRA-2 over the boxed region in (c). Additional details for all calculations are given in the text.

cell the linear regression slope of the resulting scatterplot. Positive values of, e.g., the TF_{vor} slope over a given area indicate that the TF_{vor} anomaly is typically positive there when a wave train is present (i.e., the PCA value is positive and large). For verification of the SWM results, similar regression-based maps are created from Ψ^e anomalies. Results for April wave trains that resemble REOF1 and May wave trains that resemble REOF4 are highlighted in Figs. 13 and 14 and Figs. S8 and S9, respectively. The conclusions drawn from the general case for 1980–2021 are very similar to those for 2020. In particular, TF_{vor} forcing over the North Atlantic and western Europe contributes to wave train development (Figs. 13d and S8d), and TF_{vor} forcing dominates over all other forcing types in reproducing the verification wave train patterns (Figs. 13e,f and S8e,f). Moreover, atmospheric Q anomalies do not appear to make a substantial contribution to Eurasia wave train development over the period 1980–2021 (Figs. 14 and S9).

We thus conclude that Spring 2020 was not unusual regarding the mechanisms underlying wave train development over Eurasia. The notable strength of the wave trains may be attributed, in part, to the configuration of atmospheric transient forcing over the North Atlantic and subsequent transient forcing feedbacks downstream. The anomalous North Atlantic transient circulation activity (i.e., TF_{vor} anomalies) was likely caused, to some degree, by internal atmospheric variability, potentially associated with the negative phase of the North Atlantic Oscillation.[7] Our supplementary eastern North Pacific regional replay experiment (Table S1) is unable to reproduce the observed North Atlantic TF_{vor} anomalies (not shown), explaining the lack of a Eurasia wave train in those runs (Fig. S1d) and further suggesting that the ultimate source of the North Atlantic

[7] https://www.cpc.ncep.noaa.gov/data/teledoc/nao.shtml.

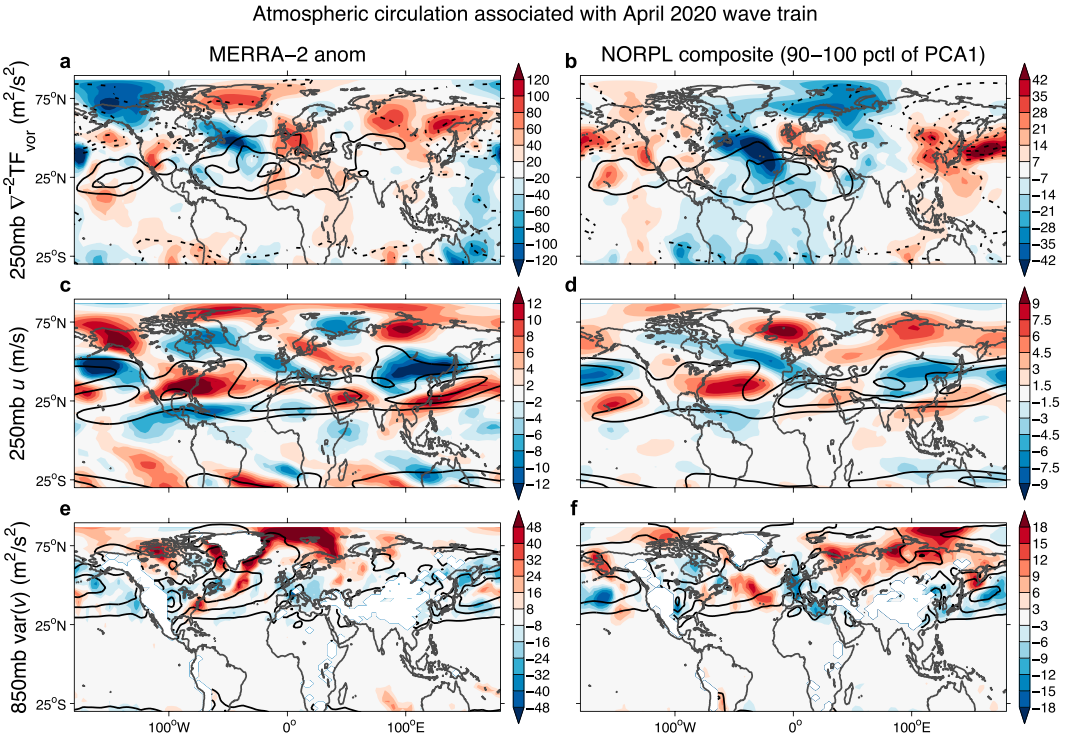

FIG. 11. Relationship between the April 2020 Eurasia wave train and atmospheric circulation metrics. (a) MERRA-2 April 2020 anomaly in the inverse Laplacian of TF_{vor} ($\nabla^{-2}TF_{vor}$) at 250 mb (shaded; $m^2\ s^{-2}$). (b) Composite of the 250-mb $\nabla^{-2}TF_{vor}$ anomaly for the NORPL 2020 ensemble members corresponding to the 90th–100th percentiles of PCA1 values (i.e., those ensemble members in which the atmospheric circulation strongly resembles the wave pattern shown in Fig. 8a). In (a) and (b), the black contours depict the 1981–2019 April climatology of 250-mb $\nabla^{-2}TF_{vor}$ for the corresponding dataset, with contours drawn every 25 $m^2\ s^{-2}$ (negative contours dashed and zero omitted). (c),(d) As in (a) and (b), but for 250-mb u ($m\ s^{-1}$), with the climatology contoured every 10 $m\ s^{-1}$ starting at 20 $m\ s^{-1}$. (e),(f) As in (a) and (b), but for the variance in 850-mb meridional wind (v), computed as $\overline{v'v'}$ ($m^2\ s^{-2}$), where the overbar is the monthly mean and primes are 6-hourly deviations from the monthly mean. Climatology contours in (e) and (f) are drawn every 25 $m^2\ s^{-2}$.

TF_{vor} forcing in 2020 was local or just upstream over the United States. The nature of the link between the North Atlantic SSTs and TF_{vor} forcing during 2020, if any, remains unclear. While our free-running AGCM experiments do not suggest the SSTs directly led to the development of the wave train forcing (Figs. 5d and 6d), we cannot rule out that coupled ocean–atmosphere processes (not captured by our model) associated with the SST gradient (Figs. 2a,c) played an important role (e.g., Chen et al. 2020; Zhang et al. 2022).

d. *Mechanisms underlying tropical–extratropical teleconnections in 2020*

We show in section 3a that tropical atmospheric forcing, potentially related to SST and precipitation anomalies, likely contributed to the anomalous warmth over Eurasia and other parts of the Northern Hemisphere during the spring of 2020 (Figs. 5c, 6c, and 7). Here, we examine the mechanisms underlying this possible teleconnection. Previous work has shown that perturbations to tropical heating [e.g., due to El Niño–Southern Oscillation (ENSO)] can impact the extratropical jet stream and atmospheric wave activity, ultimately causing zonally symmetric changes in temperature in the mid–high latitudes (Hou 1993; Chang 1995; Seager et al. 2003). In January–March 2020, the anomalously warm tropics were shown to impact the extratropics through a similar mechanism (S22). Specifically, the warm tropics induced an equatorward shift in the subtropical jet that was associated with positive anomalies of eddy momentum flux convergence near the upper branch of the Ferrel cell. The anomalous eddy flux forcing acted to strengthen the zonal wind (contributing to the positive AO) and shift the Ferrel cell poleward (causing anomalous adiabatic heating in the midlatitudes), both of which warmed the Northern Hemisphere extratropics. Did a similar teleconnection also occur during the spring of 2020? We now explore this question through a series of zonal-mean diagnostics. For simplicity, we mostly focus on the RPL_TR experiment for the period 15 April–15 May, which illustrates the tropical–extratropical teleconnection well.

Figure 15 shows zonal-mean anomalies in basic variables averaged over 15 April–15 May 2020 for RPL_TR (for reference, standardized anomalies are shown in Fig. S10). Anomalies in zonal-mean temperature ($[\overline{T}]$, where square brackets indicate the zonal mean and the overbar is the 31-day mean) are evident

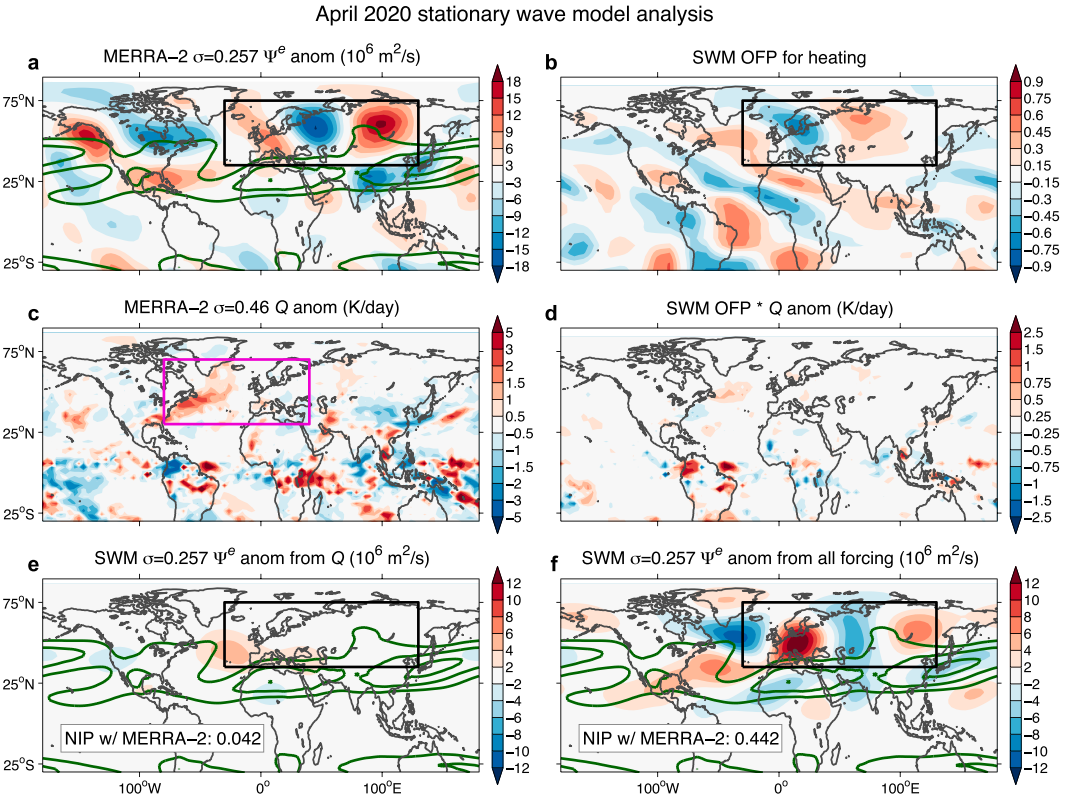

FIG. 12. As in Fig. 10, except (b) diabatic heating (Q) forcing is used to generate the optimal forcing pattern, (c) the April 2020 Q anomaly at $\sigma = 0.46$ from MERRA-2 (K day^{-1}) is shown, and (e) the SWM is run with the derived Q forcing [as shown in (c) over the region outlined with the magenta box] to produce the output. Note that Q anomalies over the entire depth of the troposphere are used as forcing for the SWM in (e), thus accounting for mid-tropospheric forcing [as shown in (c)] as well as lower-tropospheric forcing that may be influenced by SST-induced sensible and latent heat flux anomalies. (a),(f) As in Figs. 10a and 10f, respectively.

throughout the troposphere in the mid–high latitudes (between about 45° and 75°N; Fig. 15a). Another region of robust warm anomalies is the tropical upper troposphere. The tropical $[\overline{T}]$ anomalies are consistent with the anomalous precipitation during this period ultimately leading to enhanced zonal-mean condensational heating and warming in the deep tropics (Fig. S3a). As a result of larger $[\overline{T}]$ anomalies closer to the equator relative to the subtropics at a given pressure level (e.g., 300 mb), the upper-tropospheric temperature gradient increased and likely contributed to a strengthening of the subtropical jet stream (~30°N) and hence the zonal-mean zonal wind ($[\overline{u}]$) via thermal wind balance (Fig. 15b).

We also investigate the mean meridional circulation (MMC) in Fig. 15. The MMC is computed here as the pressure integral of the zonal-mean meridional wind ($[\overline{v}]$) and represents a streamfunction in the latitude–pressure plane, with positive values indicating clockwise flow and negative values counterclockwise flow. Climatological MMC values show the well-known zonal-mean circulation cells in the Northern Hemisphere: the Hadley (~5°–20°N), Ferrel (~30°–50°N), and polar (~60°–75°N) cells (Fig. 15c; Hadley 1735; Lorenz 1967). All three cells associated with the MMC were anomalous in 2020. The Hadley cell was anomalously strong (positive anomalies coinciding with climatological clockwise flow north of the equator in Fig. 15c), presumably due to the enhanced tropical precipitation (e.g., Tomassini and Yang 2022). In addition, both the Ferrel and polar cells were anomalously weak (anomalies opposite the climatological flow). By definition, the MMC anomalies were associated with anomalies in zonal-mean pressure velocity ($[\overline{\omega}]$), with a weakening of the usual ascent near 60°N and a weakening of the usual descent further north (Fig. 15d). We surmise it was this anomalous vertical motion that ultimately caused extratropical warming via adiabatic and/or diabatic processes (Chang 1995; Seager et al. 2003).

We now examine the link between the zonal jet stream and MMC anomalies. In Seager et al. (2003), a shift in the zonal jet associated with ENSO alters the meridional gradient in potential vorticity, subsequently altering the wave refraction and inducing anomalies in eddy momentum flux convergence; the anomalous eddy flux convergence then alters the MMC through the zonal-mean zonal momentum budget. We expect a similar mechanism underlies the connection between the jet and MMC anomalies in our results. To assess this, we quantify the components of the zonal-mean zonal momentum budget during the spring of 2020. As demonstrated in previous

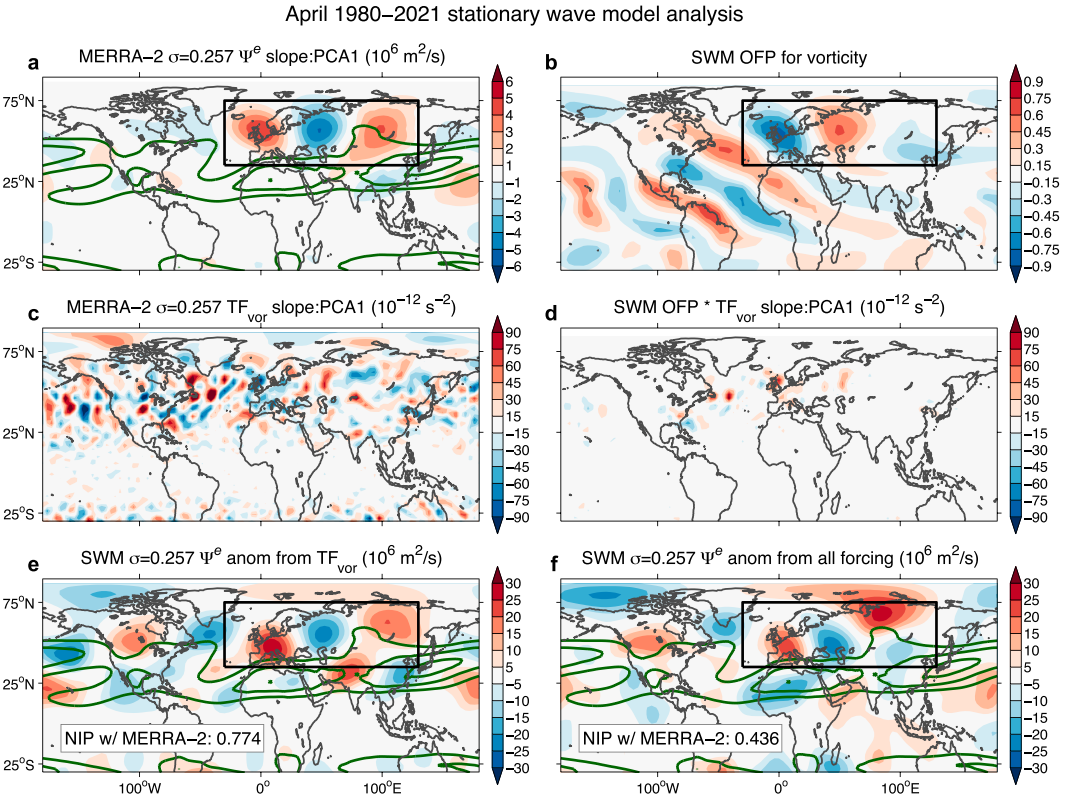

FIG. 13. As in Fig. 10, but for April wave trains that resemble REOF1 (shown in Fig. 8a) during 1980–2021. Here, the verification and forcing maps are generated by computing the linear regression slope of the MERRA-2 monthly anomalies of the corresponding quantity (Ψ^e, TF_{vor}, etc.) at each grid cell against the PCA1 values for April 1980–2021 (the latter are shown in Fig. 9c), as opposed to being computed as the April 2020 anomalies of those quantities. (e),(f) The SWM is forced with the regression-derived forcing [shown for TF_{vor} in (c)] over the entire global domain and troposphere that was first multiplied by 10 to have a similar magnitude as the April 2020 forcing (shown for TF_{vor} in Fig. 10).

studies (e.g., Seager et al. 2003) and our own analysis (not shown), there is an approximate balance in the middle and upper troposphere between the acceleration/deceleration of $[\overline{u}]$ due to horizontal eddy momentum flux convergence and its acceleration/deceleration due to the Coriolis force. Mathematically, this balance may be expressed as the following (in spherical and pressure coordinates):[8]

$$0 \sim \text{dUdt\_he} + \text{dUdt\_fV}, \tag{5}$$

$$\text{dUdt\_he} = \text{dUdt\_VUse} + \text{dUdt\_VUte}, \tag{6}$$

$$\text{dUdt\_VUse} = -\frac{1}{a\cos^2\varphi}\frac{\partial}{\partial\varphi}(\cos^2\varphi[\overline{u}^e\overline{v}^e]), \tag{7}$$

$$\text{dUdt\_VUte} = -\frac{1}{a\cos^2\varphi}\frac{\partial}{\partial\varphi}(\cos^2\varphi[\overline{u^{e\prime}v^{e\prime}}]), \quad \text{and} \tag{8}$$

$$\text{dUdt\_fV} = f[\overline{v}]\ , \tag{9}$$

where dUdt_he is the total horizontal momentum flux convergence associated with eddies [which may be separated into contributions from stationary (dUdt_VUse) and transient (dUdt_VUte) eddies], dUdt_fV is the Coriolis acceleration, a is the radius of Earth, φ is latitude, f is the Coriolis parameter, and other variables are as defined earlier. As above, the overbars represent the time mean (here, over the month-long period 15 April–15 May), the square brackets are the zonal mean, primes are the 6-hourly deviations from the time mean, and the superscript e represents the deviation from the zonal mean (or eddy). All terms represent $[\overline{u}]$ acceleration and have units of meter per squared second.

Figure 16a shows that 2020 anomalies in dUdt_he during 15 April–15 May were associated with anomalies in $[\overline{u}]$. Of note are the negative (~45°–60°N) and positive (~60°–85°N) dUdt_he anomalies in the mid–high latitudes that coincide with anomalies in $[\overline{u}]$ having the same sign. It appears the altered jet in the subtropics induces dUdt_he anomalies to the north [consistent with Seager et al. (2003)], inducing $[\overline{u}]$ anomalies in the mid–high latitudes that potentially feed back on the dUdt_he anomalies. The correspondence of positive dUdt_he and $[\overline{u}]$ anomalies north of 60°N suggests momentum

[8] See Eq. (1) in Seager et al. (2003) for the full momentum budget equation.

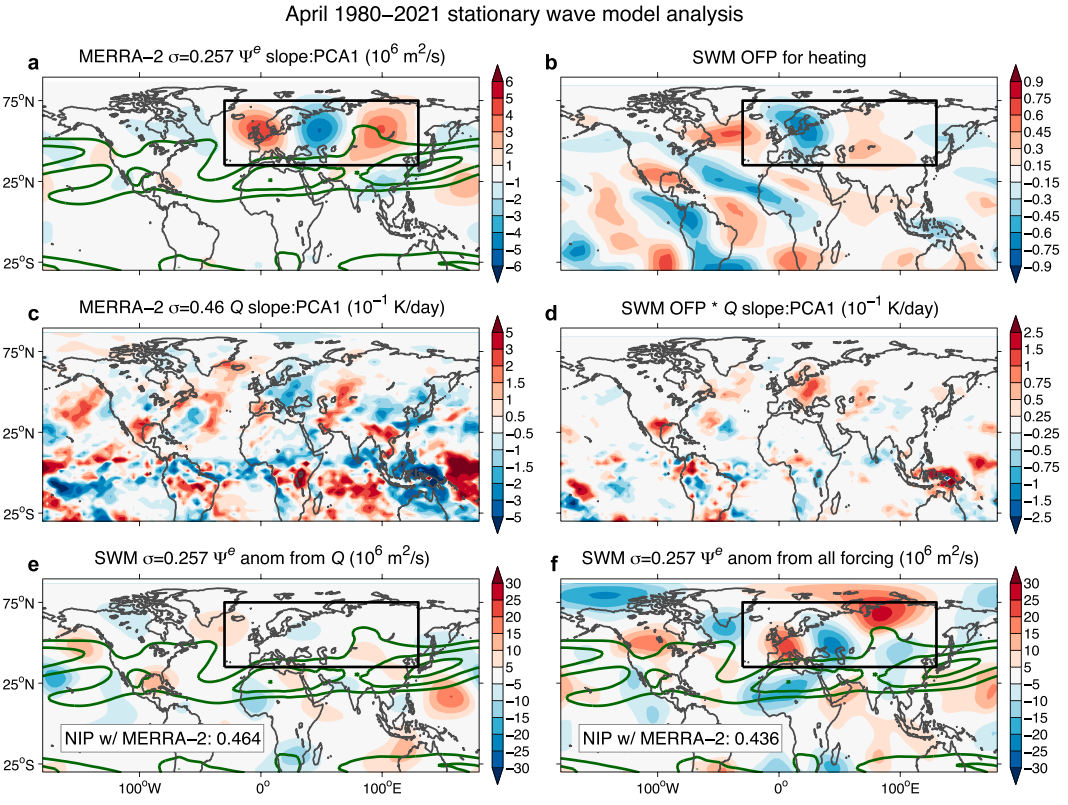

FIG. 14. As in Fig. 13, except(b) Q forcing is used to generate the optimal forcing pattern, (c) the regression slope of April Q anomalies (from MERRA-2) at $\sigma = 0.46$ against PCA1 (10^{-1} K day^{-1}) is shown, and (e) the SWM is run with the derived Q forcing over the entire globe [as shown in (c) but multiplied by 10] to produce the output. Note the Q forcing used to produce (e) is calculated for the entire troposphere, thus accounting for midtropospheric forcing [as shown in (c)] as well as lower-tropospheric forcing that may be influenced by SST-induced sensible and latent heat flux anomalies. (a),(f) As in Fig. 13a and 13f, respectively.

fluxes played a role in the positive AO from the previous winter persisting into April (Overland and Wang 2021; S22). An inspection of the stationary and transient components of dUdt_he suggests the transient eddies play a larger role (Figs. 16c,d) but that the stationary wave contribution is not negligible.

The mid–high-latitude dUdt_he anomalies are of particular interest as they are largely balanced by dUdt_fV (Fig. 16b), which is directly related to anomalies in $[\overline{v}]$ and thus the MMC [(5)–(9)]. Consequently, southerly $[\overline{v}]$ anomalies tend to occur near the upper branch of the Ferrel cell, counteracting the climatological northerly winds there (~40°N and 250 mb in Fig. 16b). Similarly, northerly $[\overline{v}]$ anomalies tend to occur near the upper branch of the polar cell, counteracting climatological southerly winds (~60°–75°N and 300 mb in Fig. 16b). To satisfy atmospheric continuity, these $[\overline{v}]$ anomalies ultimately lead to the slowing of the Ferrel and polar cells shown in Fig. 15. In summary, the momentum budget analysis in Fig. 16 is supportive of our hypothesis that the anomalies in the zonal jet stream and MMC are linked via altered wave activity and corresponding anomalies in dUdt_he. The dUdt_he anomalies, which are presumably associated with the strengthened jet due to tropical heating, provide a mechanism by which the tropics influenced the extratropics during the spring of 2020. These results are fundamentally consistent with the January–March 2020 results in S22, but with differences in how the dUdt_he anomalies qualitatively influenced the MMC due to a different placement of the former relative to the latter in the spring. That is, the dUdt_he anomalies were better positioned to weaken the Ferrel and polar cells in the spring rather than shift the Ferrel cell poleward (as happened during the prior winter). Also, we find that the transient eddies were critical during the spring, whereas S22 found stationary eddies were important during the winter. This difference is likely due to the absence of Rossby wave trains in the RPL_TR experiment (e.g., Fig. 5c), resulting in small anomalies in dUdt_VUse (7). The importance of transient eddies for the mechanism described above is consistent with the findings of Seager et al. (2003), who found a similar importance of transients for teleconnections associated with ENSO.

The next question is whether the extratropical $[\overline{T}]$ anomalies can in fact be traced to the MMC anomalies. For this

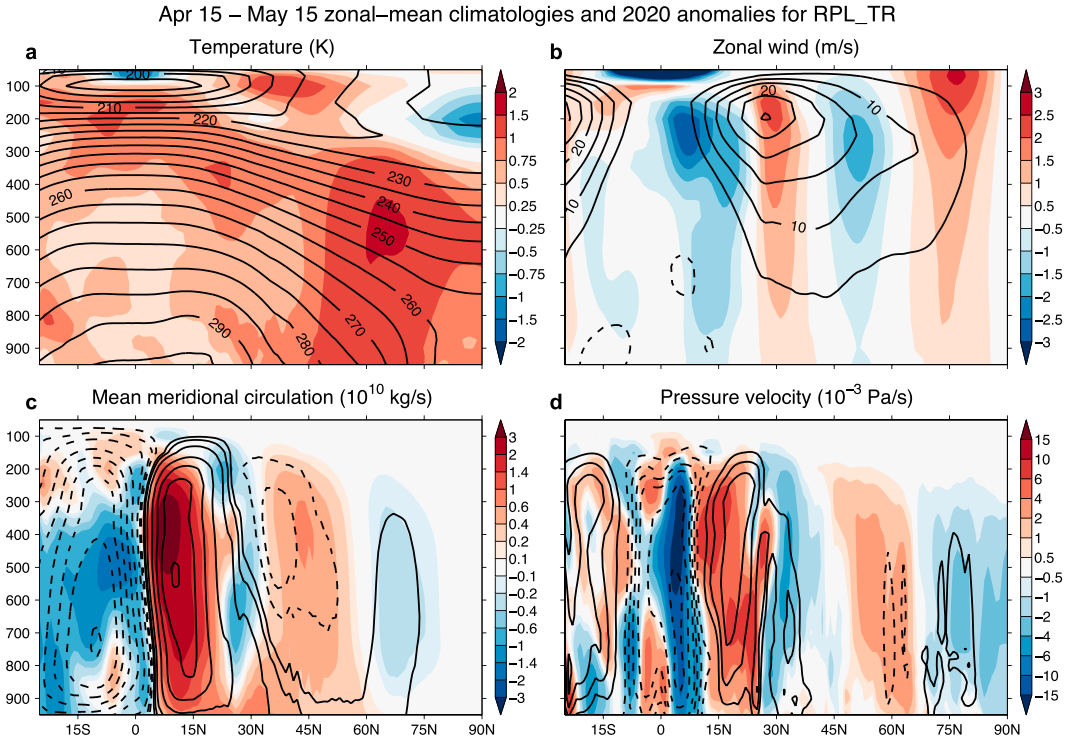

FIG. 15. Zonal-mean climatologies and 2020 anomalies of basic variables for the period 15 Apr–15 May for the RPL_TR experiment. (a) Temperature ($[\overline{T}]$) anomalies (color fill; K) and climatologies (contours). (b) Zonal wind ($[\overline{u}]$) anomalies (color fill; m s^{-1}) and climatologies (contours). (c) MMC anomalies (color fill; 10^{10} kg s^{-1}) and climatologies (contours). Contours are drawn at ± 0.5, 1, 2, 4, 6, 8, 10, 12, 15, and 20×10^{10} kg s^{-1}, with negative contours dashed. (d) Pressure velocity ($[\overline{\omega}]$) anomalies (color fill; 10^{-3} Pa s^{-1}) and climatologies (contours). Contours are drawn at ± 5, 10, 15, 20, 30, 40, 50, and 60×10^{-3} Pa s^{-1}, with negative contours dashed. The 90-member ensemble mean is shown, and the RPL_TR_CLIM 1981–2019 climatology for 15 Apr–15 May is used for generating the anomalies and for plotting the contours.

question, we assess the zonal-mean thermodynamic budget, in which there is a predominant balance between horizontal eddy heat flux convergence, vertical advection by the MMC, and diabatic heating as follows:[9]

$$0 \sim \text{dTdt\_he} + \text{dTdt\_vadv} + \text{dTdt\_Q}, \tag{10}$$

$$\text{dTdt\_he} = \text{dTdt\_VTse} + \text{dTdt\_VTte}, \tag{11}$$

$$\text{dTdt\_VTse} = -\frac{1}{a\cos\varphi}\frac{\partial}{\partial\varphi}(\cos\varphi[\overline{v}^{e}\overline{T}^{e}]), \tag{12}$$

$$\text{dTdt\_VTte} = -\frac{1}{a\cos\varphi}\frac{\partial}{\partial\varphi}(\cos\varphi[\overline{v^{e\prime}T^{e\prime}}]), \tag{13}$$

$$\text{dTdt\_vadv} = -[\overline{\omega}]\left(\frac{\partial[\overline{T}]}{\partial P} - \frac{R_d[\overline{T}]}{c_p P}\right), \quad \text{and} \tag{14}$$

$$\text{dTdt\_Q} = [\overline{Q}]\,, \tag{15}$$

where dTdt_he is the total heat flux convergence associated with eddies [which can be separated into contributions from stationary (dTdt_VTse) and transient (dTdt_VTte) eddies], dTdt_vadv is the vertical temperature advection by the zonal-mean time-mean circulation (including adiabatic effects), and dTdt_Q is diabatic heating. All terms represent $[\overline{T}]$ tendency and have units of kelvins per second.

The key thermodynamic budget terms for the period 15 April–15 May 2020 are shown in Fig. 17. As expected, the aforementioned anomalies in the MMC (and thus $[\overline{\omega}]$) are associated with anomalous dTdt_vadv, with positive anomalies (indicating anomalous adiabatic warming) coinciding with the anomalously weak ascending motion around ~60°N and anomalously warm temperatures (cf. Figs. 15d and 17b). These dTdt_vadv anomalies are balanced by both dTdt_Q and dTdt_he, the latter being strongly influenced by transients (Figs. 17a,c,d). A balancing of dTdt_vadv by both dTdt_Q and dTdt_he is consistent with Seager et al. (2003) and is indicative of two things: 1) reduced atmospheric ascent causing clearer skies and thus increased longwave radiative cooling and less condensational heating from clouds/precipitation in the midupper troposphere (i.e., a negative dTdt_Q anomaly), and 2) the role of eddies in smoothing the temperature

[9] See Eq. (2) in Seager et al. (2003) for the full temperature budget equation.

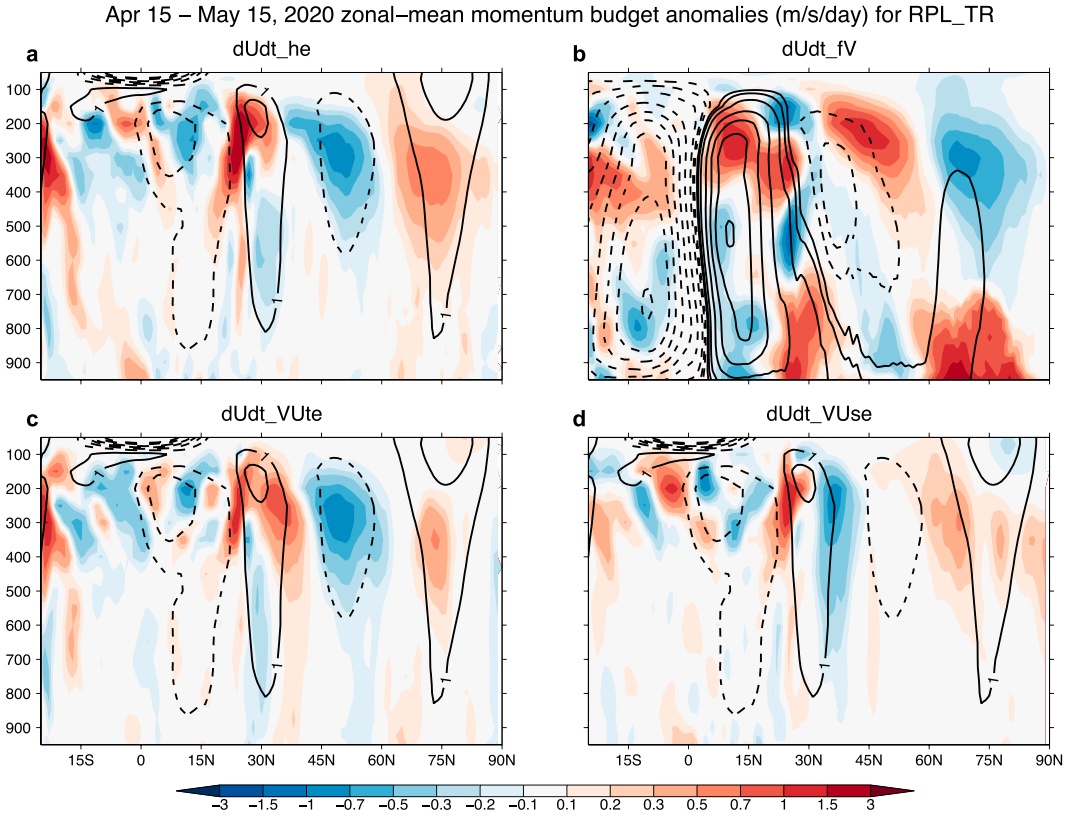

FIG. 16. Zonal-mean momentum budget analysis for 15 Apr–15 May 2020 for the RPL_TR experiment. (a) $[\overline{u}]$ tendency anomalies due to the convergence of total horizontal eddy momentum flux (dUdt_he; color fill; m s^{-1} day^{-1}). Contours of the $[\overline{u}]$ anomaly (as in Fig. 15b) are overlaid for reference. (b) $[\overline{u}]$ tendency anomalies due to the Coriolis acceleration (dUdt_fV; color fill; m s^{-1} day^{-1}). Contours of the MMC climatology (as in Fig. 15c) are overlaid. (c) As in (a), but for the component of dUdt_he due only to transient eddies (dUdt_VUte). (d) As in (a), but for the component of dUdt_he due only to stationary eddies (dUdt_VUse). All plotted quantities are defined mathematically in the text [see Eqs. (5)–(9)]. The 90-member ensemble mean is shown, and the RPL_TR_CLIM 1981–2019 climatology for 15 Apr–15 May is used for generating the anomalies and for plotting the contours. For all quantities, values are first computed for each ensemble member/year and then averaged to compute the ensemble mean or climatology.

anomalies induced by adiabatic warming (i.e., a negative dTdt_he anomaly). North of ~67°N, the balance between dTdt_vadv and dTdt_Q reverses, with the descending northern branch of the polar cell being anomalously weak and causing adiabatic cooling (Figs. 17a,b). In this latitude band, it appears diabatic heating from longwave and condensational warming is primarily responsible for the positive temperature anomalies, with dTdt_he being small south of ~83°N (Fig. 17c). Overall, these results again support our hypothesis that the warm anomalies between ~45° and 75°N are associated with anomalous heating, either adiabatic or diabatic, induced by anomalies in the MMC.

The quantities from Figs. 15–17 are shown for MERRA-2 and the NORPL experiment (alongside the RPL_TR results) in Figs. S11–S13. The results for NORPL are qualitatively similar to those for RPL_TR but with generally weaker anomalies in all fields. This is consistent with smaller tropical precipitation anomalies in NORPL and thus weaker tropical diabatic heating triggering a teleconnection mechanism (Figs. S3c and S13c). That a similar response occurs in the NORPL experiment nonetheless supports the proposition that SSTs and their impact on tropical P played a role in the tropical–extratropical teleconnection during the spring of 2020. The stationary eddy contribution to dUdt_he is larger for MERRA-2 than for the AGCM owing to the presence of Rossby wave activity (e.g., Figs. 7a and S12a,j), which evidently overwhelms the impact of the transient eddies on the MMC during the mid-April to mid-May period (Fig. S12g). Atmospheric noise likely complicates the interpretation of the MERRA-2 results, given that it is a single realization. We repeated our analysis for other subseasonal periods (including 1–15 April, 16–30 April, and the April and May monthly means) and found the AGCM results to be highly robust, but with weaker signals in May likely due to weaker extratropical baroclinicity (and thus transients) later in the spring (not shown). The MERRA-2 results are more consistent with the AGCM results for the April mean, which is likely attributable to similarly large tropical tropospheric $[\overline{T}]$ anomalies as well as dUdt_he being dominated by transients during that period (not shown). Our comparison of different subseasonal periods indicates that while

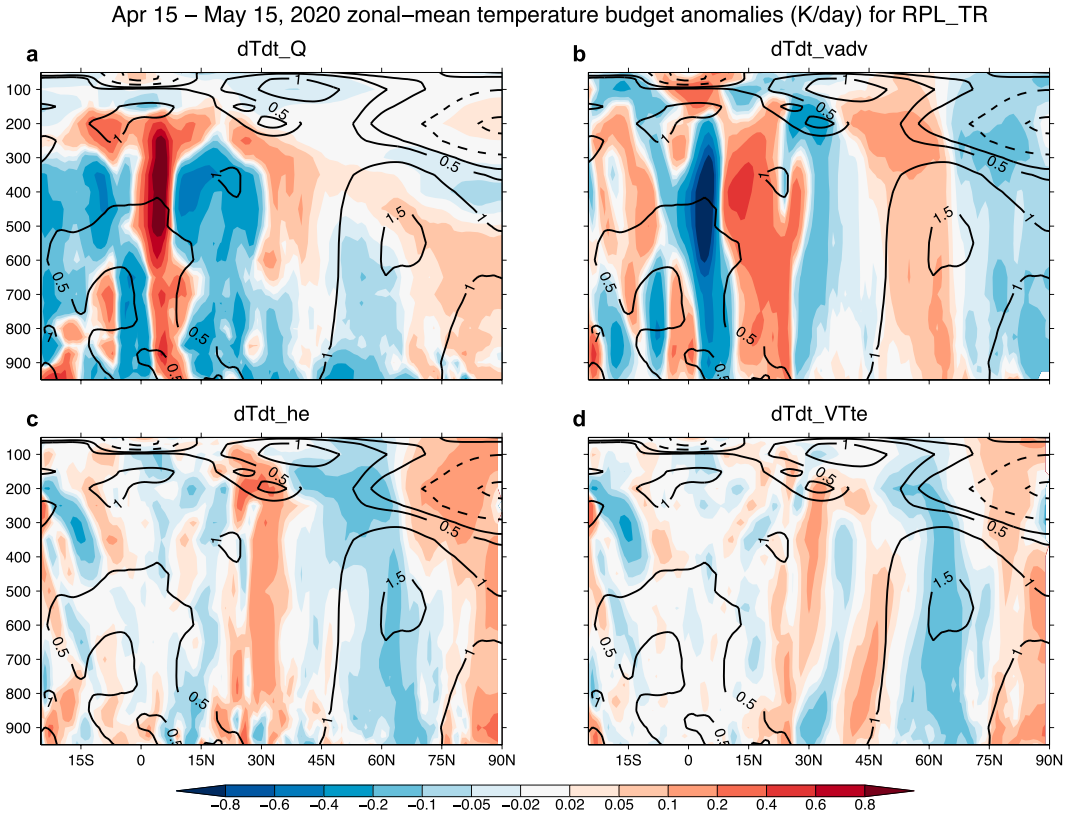

FIG. 17. Zonal-mean temperature budget analysis for 15 Apr–15 May 2020 for the RPL_TR experiment. (a) $[\overline{T}]$ tendency anomalies due to diabatic heating (dTdt_Q; color fill; K day^{-1}). (b) $[\overline{T}]$ tendency anomalies due to vertical advection and adiabatic effects from the zonal-mean time-mean circulation (dTdt_vadv; color fill; K day^{-1}). (c) $[\overline{T}]$ tendency anomalies due to the convergence of total horizontal eddy heat flux (dTdt_he; color fill; K day^{-1}). (d) As in (c), but for the component of dTdt_he due only to transient eddies (dTdt_VTte). All plotted quantities are defined mathematically in the text [(10)–(15)]. Contours of the $[\overline{T}]$ anomaly (as in Fig. 15a) are overlaid for reference on all panels. The 90-member ensemble mean is shown, and the RPL_TR_CLIM 1981–2019 climatology for 15 Apr–15 May is used for generating the anomalies. For all quantities, values are first computed for each ensemble member/year and then averaged to compute the ensemble mean or climatology.

the tropical precipitation and tropospheric $[\overline{T}]$ anomalies are physically connected, they need not follow the same temporal or geographic evolution on subseasonal time scales, consistent with earlier studies on the persistence of tropical tropospheric temperature (Kumar and Hoerling 2003; Kubota and Terao 2003; Paulik and Birner 2012).

4. Summary and discussion

We show that the unusual warmth over Siberia during April–May of 2020 can be attributed to two dynamical mechanisms: 1) persistent atmospheric ridging over northern Asia associated with Rossby wave trains emanating from the North Atlantic, and 2) a tropical–extratropical teleconnection that induced warm anomalies more broadly over the Northern Hemisphere extratropics. The April and May wave trains, which were among the strongest over the recent historical record (especially in April), were both initiated from transient vorticity flux forcing over the North Atlantic (related to enhanced storm activity) and likely sustained by the generation of additional transients associated with the wave trains themselves. While our AGCM simulations do not show a clear link between North Atlantic SST anomalies and the wave trains, it cannot be ruled out that the transient vorticity forcing over the Atlantic was linked to the underlying SST gradient and further maintained through coupled ocean–atmosphere processes. Regarding the tropical–extratropical teleconnection, the anomalously warm tropical SSTs during the spring of 2020 appear to have played an important role via the following mechanism: tropical diabatic heating anomalies associated with the warm SSTs and anomalous precipitation strengthened the subtropical jet and altered the upper-tropospheric transient eddy momentum fluxes, inducing large-scale zonal-mean atmospheric descent anomalies south of ~65°N and ascent anomalies to the north, causing adiabatic or diabatic warming, respectively.

Our AGCM results suggest the North America/North Atlantic region and tropics contributed roughly equally to the extreme warmth over Siberia in the spring of 2020 (section 3a). The observed temperature anomaly pattern over Eurasia

exhibited a clear wave structure in both April and May (Figs. 5a and 6a), presumably induced by the Rossby wave trains. We surmise teleconnections from the tropics acted to modify the local temperature anomalies associated with the wave trains (e.g., by strengthening the April warm anomaly over Siberia and suppressing the cold anomaly to its west). Other previously posited drivers of the Siberian warmth during the spring of 2020, including the lingering positive AO (Overland and Wang 2021), land–atmosphere feedbacks (Collow et al. 2022), and ozone loss (Xia et al. 2021), cannot be ruled out as also having influenced the event. In April, for instance, the lingering positive AO and tropical–extratropical teleconnection discussed here are not entirely independent (section 3d, Fig. 16a). Moreover, it cannot be ruled out that land–atmosphere feedbacks and/or ozone anomalies acted to augment the anticyclonic circulation anomalies and corresponding warmth over Siberia associated with the Rossby wave trains during both April and May, which was not explored here.

Some limitations of our study should be noted. Our conclusions are predominantly model based and thus subject to any biases or deficiencies in the GEOS model, hindering a definitive interpretation of some results. For example, we cannot rule out the possibility that the Eurasia wave train forcing was ultimately linked to the North Pacific or tropics, and that due to model error (e.g., near the boundary of replayed regions), this is not reflected in the AGCM results (e.g., Fig. S1). It is also difficult to know conclusively whether North Atlantic SSTs played an important role in the wave train generation due to possible errors in the atmospheric response to these SSTs. On that note, our use of prescribed SSTs imposes additional limitations. For one, our experiments cannot address whether coupled atmosphere–ocean processes are important. Also, prescribing SSTs everywhere does not allow for the isolation of SST contributions from individual basins/regions. Nevertheless, we have reason to expect that the model used here is sufficiently reliable and provides meaningful results. For instance, the tendency bias correction applied (section 2b) has been shown to substantially improve the GEOS model climate biases (Chang et al. 2019, 2021; Schubert et al. 2019b), and those improvements are robust when the model is run at coarser resolution (not shown). We also corrected for model climate biases that may have been introduced by regional replay (section 2b; Table 1). Finally, the AGCM does adequately capture the atmospheric dynamics associated with the 2020 Eurasia Rossby wave trains, a key aspect of this paper (e.g., Fig. 11).

Given the variety of mechanisms shown to be important for the unusual Siberian warmth during the spring of 2020, the potential subseasonal predictability (i.e., at 2–6-week lead) of this and similar events is an open and interesting question. Successful prediction of such an event, particularly its zonally asymmetric temperature anomaly structure, would require successfully predicting the Rossby wave trains that drive it. Since the wave trains are shown here to be forced by transient atmospheric circulations (i.e., subdaily- to synoptic-scale fluctuations), this would require the accurate prediction of those transients at long-enough lead times for the wave trains to develop. Even if the transients are influenced by persistent underlying SST anomalies, as previously suggested over the North Atlantic (e.g., Zhang et al. 2022), predicting the correct placement and timing of the Rossby wave source would pose a significant challenge. This is because atmospheric transients are inevitably generated by internal variability, which has an inherent predictability limit (e.g., Zhang et al. 2019). Furthermore, accurate wave train prediction also relies on the forecast model's accurate representation of the background state and transient eddy feedbacks, which is not guaranteed (Wang et al. 2017; Chen et al. 2021). It therefore seems unlikely that Rossby wave trains of the character discussed here would be predictable beyond the weather prediction (i.e., 7–10-day) time frame, limiting predictability of the heatwaves they induce. On the other hand, predictability stemming from the more slowly varying boundary conditions (e.g., tropical SSTs or local land surface anomalies), shown to also be important for such extreme temperature events, may be more promising (e.g., DeAngelis et al. 2020; Koster et al. 2021).

Finally, the potential influence of climate change on the unusual Siberian warmth during the spring of 2020 cannot be overlooked. A connection between anthropogenic warming and the 2020 Siberian heat has been shown in a recent in-depth statistical study (Ciavarella et al. 2021), though the physical pathway by which this connection occurred was not proposed. We demonstrate here that above-average tropical temperatures, both at the surface and in the troposphere, might have induced extratropical temperature anomalies through modifications to the zonal-mean circulation. Furthermore, tropical temperature anomalies in 2020 were strongly influenced by warming trends over the past 40 years (cf. Figs. 2, 15a, and S14a), which were themselves strongly associated with trends in tropical precipitation (not shown). To the extent the observed tropical trends were anthropogenic in nature, part of the zonal-mean tropical–extratropical teleconnection discussed here could be linked to human-induced climate change. Extratropical trends in dynamical metrics related to this teleconnection were not found (cf. Figs. 15b–d and S14b–d), but this could be because other processes, potentially related to extratropical SSTs, influenced those trends as well. Additional study of the tropical–extratropical teleconnection presented here within the framework of a larger anthropogenic signal (e.g., large-ensemble future climate simulations) or controlled perturbations to the system (e.g., imposing only tropical boundary forcing) could help clarify the role of climate change in Siberian heatwave generation, as could experiments targeting anthropogenic impacts on springtime Rossby wave trains. Such additional research could prove valuable for enhancing our physical understanding of temperature extremes in a changing climate.

Acknowledgments. This work was supported by the National Climate Assessment Enabling Tools project at NASA's GMAO and by the NASA MAP program (80NSSC21K1729). MERRA-2 data were developed by the NASA GMAO at the GSFC under funding by the NASA MAP program. Computational resources supporting this work were provided by the NASA HEC program through the NASA NCCS at GSFC.

We thank Mike Bosilovich and Natalie Thomas for useful discussions on the topic.

Data availability statement. MERRA-2 data are available from the GES DISC at https://disc.gsfc.nasa.gov. Output from the AGCM simulations can be made available upon request.

REFERENCES

Ambrizzi, T., B. J. Hoskins, and H.-H. Hsu, 1995: Rossby wave propagation and teleconnection patterns in the austral winter. *J. Meteor.*, **52**, 3661–3672, https://doi.org/10.1175/1520-0469(1995)052<3661:RWPATP>2.0.CO;2.

Barnston, A. G., and R. E. Livezey, 1987: Classification, seasonality and persistence of low-frequency atmospheric circulation patterns. *Mon. Wea. Rev.*, **115**, 1083–1126, https://doi.org/10.1175/1520-0493(1987)115<1083:CSAPOL>2.0.CO;2.

Binder, H., M. Boettcher, H. Joos, and H. Wernli, 2016: The role of warm conveyor belts for the intensification of extratropical cyclones in Northern Hemisphere winter. *J. Atmos. Sci.*, **73**, 3997–4020, https://doi.org/10.1175/JAS-D-15-0302.1.

Bosilovich, M. G., and Coauthors, 2015: MERRA-2: Initial evaluation of the climate. NASA Tech. Memo. NASA/TM-2015-104606, Vol. 43, 145 pp., https://gmao.gsfc.nasa.gov/pubs/docs/Bosilovich803.pdf.

——, R. Lucchesi, and M. Suarez, 2016: MERRA-2: File specification. GMAO Office Note 9 (version 1.1), 73 pp., https://gmao.gsfc.nasa.gov/pubs/docs/Bosilovich785.pdf.

——, F. R. Robertson, L. Takacs, A. Molod, and D. Mocko, 2017: Atmospheric water balance and variability in the MERRA-2 reanalysis. *J. Climate*, **30**, 1177–1196, https://doi.org/10.1175/JCLI-D-16-0338.1.

Chang, E. K. M., 1995: The influence of Hadley circulation intensity changes on extratropical climate in an idealized model. *J. Meteor.*, **52**, 2006–2024, https://doi.org/10.1175/1520-0469(1995)052<2006:TIOHCI>2.0.CO;2.

Chang, Y., S. D. Schubert, R. D. Koster, A. M. Molod, and H. Wang, 2019: Tendency bias correction in coupled and uncoupled global climate models with a focus on impacts over North America. *J. Climate*, **32**, 639–661, https://doi.org/10.1175/JCLI-D-18-0598.1.

——, ——, ——, and ——, 2021: Tendency bias correction in the GEOS AGCM. NASA Tech. Memo. NASA/TM-2021-104606, Vol. 57, 71 pp., https://gmao.gsfc.nasa.gov/pubs/docs/Chang1326.pdf.

Chen, S., R. Wu, and Y. Liu, 2016: Dominant modes of interannual variability in Eurasian surface air temperature during boreal spring. *J. Climate*, **29**, 1109–1125, https://doi.org/10.1175/JCLI-D-15-0524.1.

——, ——, W. Chen, K. Hu, and B. Yu, 2020: Structure and dynamics of a springtime atmospheric wave train over the North Atlantic and Eurasia. *Climate Dyn.*, **54**, 5111–5126, https://doi.org/10.1007/s00382-020-05274-7.

——, ——, and ——, 2021: Influence of North Atlantic sea surface temperature anomalies on springtime surface air temperature variation over Eurasia in CMIP5 models. *Climate Dyn.*, **57**, 2669–2686, https://doi.org/10.1007/s00382-021-05826-5.

Ciavarella, A., and Coauthors, 2021: Prolonged Siberian heat of 2020 almost impossible without human influence. *Climatic Change*, **166**, 9, https://doi.org/10.1007/s10584-021-03052-w.

Collow, A. B. M., N. P. Thomas, M. G. Bosilovich, Y.-K. Lim, S. D. Schubert, and R. D. Koster, 2022: Seasonal variability in the mechanisms behind the 2020 Siberian heatwaves. *J. Climate*, **35**, 3075–3090, https://doi.org/10.1175/JCLI-D-21-0432.1.

DeAngelis, A. M., H. Wang, R. D. Koster, S. D. Schubert, Y. Chang, and J. Marshak, 2020: Prediction skill of the 2012 U.S. Great Plains flash drought in subseasonal experiment (SubX) models. *J. Climate*, **33**, 6229–6253, https://doi.org/10.1175/JCLI-D-19-0863.1.

Ding, Q., and B. Wang, 2005: Circumglobal teleconnection in the Northern Hemisphere summer. *J. Climate*, **18**, 3483–3505, https://doi.org/10.1175/JCLI3473.1.

Fragkoulidis, G., V. Wirth, P. Bossmann, and A. H. Fink, 2018: Linking Northern Hemisphere temperature extremes to Rossby wave packets. *Quart. J. Roy. Meteor. Soc.*, **144**, 553–566, https://doi.org/10.1002/qj.3228.

Gelaro, R., and Coauthors, 2017: The modern-era retrospective analysis for research and applications, version 2 (MERRA-2). *J. Climate*, **30**, 5419–5454, https://doi.org/10.1175/JCLI-D-16-0758.1.

GMAO, 2015a: tavg1_2d_slv_Nx hourly collection. Goddard Space Flight Center Distributed Active Archive Center (GSFC DAAC), accessed 1 February 2021, https://doi.org/10.5067/VJAFPLI1CSIV.

——, 2015b: tavg1_2d_flx_Nx hourly collection. Goddard Space Flight Center Distributed Active Archive Center (GSFC DAAC), accessed 1 February 2021, https://doi.org/10.5067/7MCPBJ41Y0K6.

——, 2015c: inst3_3d_asm_Np 3-hourly collection. Goddard Space Flight Center Distributed Active Archive Center (GSFC DAAC), accessed 1 February 2021, https://doi.org/10.5067/QBZ6MG944HW0.

——, 2015d: tavg3_3d_tdt_Np 3-hourly collection. Goddard Space Flight Center Distributed Active Archive Center (GSFC DAAC), accessed 1 February 2021, https://doi.org/10.5067/9NCR9DDDOPFI.

Hadley, G., 1735: Concerning the cause of the general trade-winds. *Philos. Trans. Roy. Soc..*, **29**, 58–62, https://doi.org/10.1098/rstl.1735.0014.

Hoskins, B. J., and T. Ambrizzi, 1993: Rossby wave propagation on a realistic longitudinally varying flow. *J. Atmos. Sci.*, **50**, 1661–1671, https://doi.org/10.1175/1520-0469(1993)050<1661:RWPOAR>2.0.CO;2.

Hou, A. Y., 1993: The influence of tropical heating displacements on the extratropical climate. *J. Atmos. Sci.*, **50**, 3553–3570, https://doi.org/10.1175/1520-0469(1993)050<3553:TIOTHD>2.0.CO;2.

Koster, R. D., A. M. DeAngelis, S. D. Schubert, and A. M. Molod, 2021: Asymmetry in subseasonal surface air temperature forecast error with respect to soil moisture initialization. *J. Hydrometeor.*, **22**, 2505–2519, https://doi.org/10.1175/JHM-D-21-0022.1.

Kubota, T., and T. Terao, 2003: The seasonal-scale persistence of tropical tropospheric temperature associated with the El Niño/Southern Oscillation. *J. Meteor. Soc. Japan*, **81**, 581–598, https://doi.org/10.2151/jmsj.81.581.

Kumar, A., and M. P. Hoerling, 2003: The nature and causes for the delayed atmospheric response to El Niño. *J. Climate*, **16**, 1391–1403, https://doi.org/10.1175/1520-0442(2003)16<1391:TNACFT>2.0.CO;2.

Lim, Y.-K., 2015: The east Atlantic/west Russia (EA/WR) teleconnection in the North Atlantic: Climate impact and relation to Rossby wave propagation. *Climate Dyn.*, **44**, 3211–3222, https://doi.org/10.1007/s00382-014-2381-4.

Liu, A. Z., M. Ting, and H. Wang, 1998: Maintenance of circulation anomalies during the 1988 drought and 1993 floods over the United States. *J. Atmos. Sci.*, **55**, 2810–2832, https://doi.org/10.1175/1520-0469(1998)055<2810:MOCADT>2.0.CO;2.

Liu, Y., L. Wang, W. Zhou, and W. Chen, 2014: Three Eurasian teleconnection patterns: Spatial structures, temporal variability, and associated winter climate anomalies. *Climate Dyn.*, **42**, 2817–2839, https://doi.org/10.1007/s00382-014-2163-z.

Lorenz, E. N., 1967: The nature and theory of the general circulation of the atmosphere. World Meteorological Organization Tech. Doc. 218, 161 pp., https://library.wmo.int/doc_num.php?explnum_id=10889.

Ma, Q., and C. L. E. Franzke, 2021: The role of transient eddies and diabatic heating in the maintenance of European heat waves: A nonlinear quasi-stationary wave perspective. *Climate Dyn.*, **56**, 2983–3002, https://doi.org/10.1007/s00382-021-05628-9.

McCarty, W., L. Coy, R. Gelaro, A. Huang, D. Merkova, E. B. Smith, M. Sienkiewicz, and K. Wargan, 2016: MERRA-2 input observations: Summary and assessment. NASA Tech. Memo. NASA/TM-2016-104606, Vol. 46, 61 pp., https://gmao.gsfc.nasa.gov/pubs/docs/McCarty885.pdf.

Meng, M., D. Gong, T. Zhu, P. Yao, and T. Zhou, 2022: Significant association between winter North Atlantic SST and spring NDVI anomaly over Eurasia. *J. Geophys. Res. Atmos.*, **127**, e2021JD036315, https://doi.org/10.1029/2021JD036315.

Molod, A., L. Takacs, M. Suarez, and J. Bacmeister, 2015: Development of the GEOS-5 atmospheric general circulation model: Evolution from MERRA to MERRA2. *Geosci. Model Dev.*, **8**, 1339–1356, https://doi.org/10.5194/gmd-8-1339-2015.

Overland, J. E., and M. Wang, 2021: The 2020 Siberian heat wave. *Int. J. Climatol.*, **41**, E2341–E2346, https://doi.org/10.1002/joc.6850.

Paulik, L. C., and T. Birner, 2012: Quantifying the deep convective temperature signal within the tropical tropopause layer (TTL). *Atmos. Chem. Phys.*, **12**, 12 183–12 195, https://doi.org/10.5194/acp-12-12183-2012.

Pfahl, S., E. Madonna, M. Boettcher, H. Joos, and H. Wernli, 2014: Warm conveyor belts in the ERA-Interim dataset (1979–2010). Part II: Moisture origin and relevance for precipitation. *J. Climate*, **27**, 27–40, https://doi.org/10.1175/JCLI-D-13-00223.1.

Randles, C. A., and Coauthors, 2016: The MERRA-2 aerosol assimilation. NASA Tech. Memo. NASA/TM-2016-104606, Vol. 45, 152 pp., https://gmao.gsfc.nasa.gov/pubs/docs/Randles887.pdf.

Reichle, R. H., and Q. Liu, 2014: Observation-corrected precipitation estimates in GEOS-5. NASA Tech. Memo. NASA/TM-2014-104606, Vol. 35, 18 pp., https://ntrs.nasa.gov/archive/nasa/casi.ntrs.nasa.gov/20150000725.pdf.

——, ——, R. D. Koster, C. S. Draper, S. P. P. Mahanama, and G. S. Partyka, 2017: Land surface precipitation in MERRA-2. *J. Climate*, **30**, 1643–1664, https://doi.org/10.1175/JCLI-D-16-0570.1.

Richman, M. B., 1986: Rotation of principal components. *Int. J. Climatol.*, **6**, 293–335, https://doi.org/10.1002/joc.3370060305.

Röthlisberger, M., L. Frossard, L. F. Bosart, D. Keyser, and O. Martius, 2019: Recurrent synoptic-scale Rossby wave patterns and their effect on the persistence of cold and hot spells. *J. Climate*, **32**, 3207–3226, https://doi.org/10.1175/JCLI-D-18-0664.1.

Schubert, S. D., H. Wang, and M. J. Suarez, 2011: Warm season subseasonal variability and climate extremes in the Northern Hemisphere: The role of stationary Rossby waves. *J. Climate*, **24**, 4773–4792, https://doi.org/10.1175/JCLI-D-10-05035.1.

——, ——, R. D. Koster, M. J. Suarez, and P. Y. Groisman, 2014: Northern Eurasian heat waves and droughts. *J. Climate*, **27**, 3169–3207, https://doi.org/10.1175/JCLI-D-13-00360.1.

——, A. Borovikov, Y.-K. Lim, and A. Molod, 2019a: Ensemble generation strategies employed in the GMAO GEOS-S2S forecast system. NASA Tech. Memo. NASA/TM-2019-104606, Vol. 53, 73 pp., https://gmao.gsfc.nasa.gov/pubs/docs/Schubert1183.pdf.

——, Y. Chang, H. Wang, R. D. Koster, and A. M. Molod, 2019b: A systematic approach to assessing the sources and global impacts of errors in climate models. *J. Climate*, **32**, 8301–8321, https://doi.org/10.1175/JCLI-D-19-0189.1.

——, ——, A. M. DeAngelis, H. Wang, and R. D. Koster, 2021: On the development and demise of the fall 2019 southeast U.S. flash drought: Links to an extreme positive IOD. *J. Climate*, **34**, 1701–1723, https://doi.org/10.1175/JCLI-D-20-0428.1.

——, ——, ——, R. D. Koster, Y.-K. Lim, and H. Wang, 2022: Exceptional warmth in the Northern Hemisphere during January through March of 2020: The roles of unforced and forced modes of atmospheric variability. *J. Climate*, **35**, 2565–2584, https://doi.org/10.1175/JCLI-D-21-0291.1.

Seager, R., N. Harnik, Y. Kushnir, W. Robinson, and J. Miller, 2003: Mechanisms of hemispherically symmetric climate variability. *J. Climate*, **16**, 2960–2978, https://doi.org/10.1175/1520-0442(2003)016<2960:MOHSCV>2.0.CO;2.

Ting, M., and L. Yu, 1998: Steady response to tropical heating in wavy linear and nonlinear baroclinic models. *J. Atmos. Sci.*, **55**, 3565–3582, https://doi.org/10.1175/1520-0469(1998)055<3565:SRTTHI>2.0.CO;2.

——, H. Wang, and L. Yu, 2001: Nonlinear stationary wave maintenance and seasonal cycle in the GFDL R30 GCM. *J. Atmos. Sci.*, **58**, 2331–2354, https://doi.org/10.1175/1520-0469(2001)058<2331:NSWMAS>2.0.CO;2.

Tomassini, L., and G.-Y. Yang, 2022: Tropical moist convection as an important driver of Atlantic Hadley circulation variability. *Quart. J. Roy. Meteor. Soc.*, **148**, 3287–3302, https://doi.org/10.1002/qj.4359.

Wallace, J. M., and D. S. Gutzler, 1981: Teleconnections in the geopotential height field during the Northern Hemisphere winter. *Mon. Wea. Rev.*, **109**, 784–812, https://doi.org/10.1175/1520-0493(1981)109<0784:TITGHF>2.0.CO;2.

Wang, H., S. D. Schubert, and R. D. Koster, 2017: North American drought and links to northern Eurasia: The role of stationary Rossby waves. *Climate Extremes: Patterns and Mechanisms*, *Geophys. Monogr.*, Vol. 226, Amer. Geophys. Union, 197–221.

Wu, R., and S. Chen, 2020: What leads to persisting surface air temperature anomalies from winter to following spring over mid- to high-latitude Eurasia? *J. Climate*, **33**, 5861–5883, https://doi.org/10.1175/JCLI-D-19-0819.1.

Xia, Y., Y. Hu, Y. Huang, C. Zhao, F. Xei, and Y. Yang, 2021: Significant contribution of severe ozone loss to the Siberian–Arctic surface warming in spring 2020. *Geophys. Res. Lett.*, **48**, e2021GL092509, https://doi.org/10.1029/2021GL092509.

Zhang, F., Y. Q. Sun, L. Magnusson, R. Buizza, S.-J. Lin, J.-H. Chen, and K. Emanuel, 2019: What is the predictability limit of midlatitude weather? *J. Atmos. Sci.*, **76**, 1077–1091, https://doi.org/10.1175/JAS-D-18-0269.1.

Zhang, M., J. Sun, and Y. Gao, 2022: Impacts of North Atlantic sea surface temperature on the predominant modes of spring precipitation monthly evolution over northeast China. *Climate Dyn.*, **58**, 1383–1401, https://doi.org/10.1007/s00382-021-05966-8.